Intercomparison and evaluation of cumulus parametrizations under summertime midlatitude continental conditions

By SHAOCHENG XIE[1]*, KUAN-MAN XU[2], RICHARD T. CEDERWALL[1], PETER BECHTOLD[3], ANTHONY D. DEL GENIO[4], STEPHEN A. KLEIN[5], DOUGLAS G. CRIPE[6], STEVEN J. GHAN[7], DAVID GREGORY[8], SAM F. IACOBELLIS[9], STEVEN K. KRUEGER[10], ULRIKE LOHMANN[11], JON C. PETCH[12], DAVID A. RANDALL[6], LEON D. ROTSTAYN[13], RICHARD C. J. SOMERVILLE[9], YOGESH C. SUD[14], KNUT VON SALZEN[15], GREGORY K. WALKER[14], AUDREY WOLF[4], J. JOHN YIO[1], GUANG JUN ZHANG[9] and MINGHUA ZHANG[16]

[1]*Lawrence Livermore National Laboratory, USA*
[2]*NASA Langley Research Center, USA*
[3]*Observatoire Midi-Pyrenees, France*
[4]*NASA Goddard Institute for Space Studies, USA*
[5]*NOAA Geophysical Fluid Dynamics Laboratory, USA*
[6]*Colorado State University, USA*
[7]*Pacific Northwest National Laboratory, USA*
[8]*European Centre for Medium-Range Weather Forecasts, UK*
[9]*Scripps Institution of Oceanography, University of California, USA*
[10]*University of Utah, USA*
[11]*Dalhousie University, Canada*
[12]*Met Office, UK*
[13]*CSIRO Atmospheric Research, Australia*
[14]*Goddard Space Flight Center, USA*
[15]*Canadian Center for Climate Modeling and Analysis, University of Victoria, Canada*
[16]*State University of New York at Stony Brook, USA*

SUMMARY

This study reports the Single-Column Model (SCM) part of the Atmospheric Radiation Measurement (ARM)/the Global Energy and Water Cycle Experiment (GEWEX) Cloud System Study (GCSS) joint SCM and Cloud-Resolving Model (CRM) Case 3 intercomparison study, with a focus on evaluation of cumulus parametrizations used in SCMs. Fifteen SCMs are evaluated under summertime midlatitude continental conditions using data collected at the ARM Southern Great Plains site during the summer 1997 Intensive Observing Period. Results from ten CRMs are also used to diagnose problems in the SCMs.

It is shown that most SCMs can generally capture well the convective events that were well-developed within the SCM domain, while most of them have difficulties in simulating the occurrence of those convective events that only occurred within a small part of the domain. All models significantly underestimate the surface stratiform precipitation. A third of them produce large errors in surface precipitation and thermodynamic structures. Deficiencies in convective triggering mechanisms are thought to be one of the major reasons. Using a triggering mechanism that is based on the vertical integral of parcel buoyant energy without additional appropriate constraints results in overactive convection, which in turn leads to large systematic warm/dry biases in the troposphere. It is also shown that a non-penetrative convection scheme can underestimate the depth of instability for midlatitude convection, which leads to large systematic cold/moist biases in the troposphere.

SCMs agree well quantitatively with CRMs in the updraught mass fluxes, while most models significantly underestimate the downdraught mass fluxes. Neglect of mesoscale updraught and downdraught mass fluxes in the SCMs contributes considerably to the discrepancies between the SCMs and the CRMs. In addition, uncertainties in the diagnosed mass fluxes in the CRMs and deficiencies with cumulus parametrizations are not negligible.

Similar results are obtained in the sensitivity tests when different forcing approaches are used. Finally, sensitivity tests from an SCM indicate that its simulations can be greatly improved when its triggering mechanism and closure assumption are improved.

KEYWORDS: Continental cumulus convection   Single-column models

1. INTRODUCTION

Parametrization of physical processes associated with cumulus convection, radiation and cloud formation in general circulation models (GCMs) has proven to be extremely

challenging, largely because it involves complicated scale interactions among different processes that are not well understood. Given the large uncertainties in parametrizations, a systematic evaluation and an intercomparison of the parametrization schemes used in different GCMs are essential steps in further developing and improving parametrizations. For this purpose, the ARM[*] Cloud Parameterization and Modeling (CPM) Working Group (WG) and the GCSS[†] WG 4 have conducted a series of model intercomparison case-studies using data collected from the ARM Southern Great Plains (SGP) Cloud and Radiation Testbed (CART) site and other field measurements (e.g. TOGA COARE[‡]; Webster and Lukas 1992).

The Single-Column Model (SCM) and Cloud-Resolving Model (CRM) are two approaches used to test and develop parametrizations in the intercomparison studies (Browning 1994; Randall *et al.* 1996). An SCM represents a grid column of a GCM, where the large-scale advective tendencies are specified from observations and/or large-scale models, and the model parametrizations are integrated forward in time. The simulated results can then be compared to observations. A CRM is a model with sufficient resolution to resolve the dynamical structures of cloud systems. It is designed to explicitly simulate the cloud-scale processes that must be parametrized in a GCM or SCM. Since CRMs can compute some fields that are very difficult to observe, such as the vertical distributions of cumulus mass fluxes and liquid water and ice, results from CRMs are useful to diagnose problems with SCMs. However, CRMs contain parametrizations such as cloud microphysics and turbulence. Thus, their results need to be used cautiously.

The earlier intercomparison case-studies include a midlatitude continental case (Case 1) conducted by ARM CPM WG and two tropical oceanic cases conducted by GCSS WG 4. The midlatitude continental case-study uses data collected from the ARM SGP CART site during the summer 1995 Intensive Operational Period (IOP; Ghan *et al.* 2000). Ghan *et al.* (2000) focuses on evaluating different methodologies such as the objective analysis methods for deriving large-scale advective tendencies, large-scale forcing methods for use in SCMs and CRMs and the methods used to estimate surface flux forcing.

The two GCSS case-studies are both based on data collected during the TOGA COARE IOP. The first case-study focuses on the detailed study of a squall line on a time-scale of hours. Results from CRMs are compared with kinematic and radar reflectivity observations from airborne Doppler radar (Redelsperger *et al.* 2000). The SCMs are forced by temperature and moisture tendencies computed from a reference CRM simulation, and SCM results are evaluated by outputs from the reference CRM (Bechtold *et al.* 2000). The second GCSS case simulates the multi-day evolution of cloud systems during the 20–26 December 1992 subperiod, driven by the observed large-scale forcing and sea surface temperature (Krueger *et al.* 2002). The consensus of both SCM and CRM simulated results is compared against available observations.

In line with these earlier case-studies, the ARM CPM WG and the GCSS WG 4 have conducted a joint SCM and CRM Case 3 intercomparison study, based on the data collected from the ARM SGP site during the summer 1997 IOP (Cederwall *et al.* 2000). Compared with the earlier cases, the Case 3 study is aimed at advancing the understanding of midlatitude continental convection. It also involves more CRMs (ten) and SCMs (fifteen) compared to the earlier studies. In addition, this study breaks the IOP

---

[*] Atmospheric Radiation Measurement program (Stokes and Schwartz 1994).
[†] Global Energy and Water Cycle Experiment (GEWEX) Cloud System Study.
[‡] Tropical Ocean–Global Atmosphere Coupled Ocean–Atmosphere Response Experiment.

into several short subperiods with each lasting for 4 or 5 days, based on different weather conditions, to avoid the problem of simulations that drift away from observations over long time integrations (Ghan *et al.* 2000) and to make the evaluation more meaningful, especially for SCMs.

The present work reports the SCM part of the Case 3 intercomparison study. The CRM results are described in a companion paper (Xu *et al.* 2002). The focus of the current paper is on the evaluation of cumulus parametrizations used in SCMs. This is motivated by the critical role of cumulus convection in large-scale circulations. Besides, a detailed analysis of cumulus parametrizations can help better understand SCM simulations that are usually difficult to interpret because of uncertainties in both the observed large-scale input data and the model parametrizations (Ghan *et al.* 2000).

Evaluation of individual cumulus parametrizations can be found in many early studies (e.g. Lord and Arakawa 1982; Grell *et al.* 1991; Xu and Arakawa 1992). Most of them use data obtained from tropical oceanic regions, such as the GATE* dataset (Thompson *et al.* 1979). This is partly due to inadequate field measurements in the midlatitudes. There are significant differences between the environments of the tropical and midlatitude continental convective systems such as: the underlying surface, the moisture content in the atmospheric column, the depth of the subcloud layers and instability/inhibition as summarized in Xu and Randall (2000). Extratropical summertime convection is significantly different from tropical convection. For example, extratropical convection can be formed by the lifting of a potentially unstable layer of upper air rather than of the near-surface air. Ogura and Jiang (1985) and Wu (1993) showed that deep clouds dominate the cloud population in the midlatitude convective systems. Therefore, some assumptions made in the parametrizations based on tropical observations may not be suitable for use over midlatitude continents. For example, Xie and Zhang (2000) evaluated the deep convection scheme used in the NCAR† Community Climate Model version 3 (CCM3) using the ARM SGP data. They found that the use of a positive CAPE (convective available potential energy) to trigger convection resulted in an overestimation of convection during the daytime and underestimation during the night-time due to the strong diurnal heating that controls the variation of CAPE. Thus, validation of cumulus parametrizations against the midlatitude data is a necessary step for further improvements of cumulus parametrizations.

In this paper, we compare and evaluate cumulus parametrizations in 15 SCMs using the ARM SGP summer 1997 IOP data, which covers several continental convective events. The purpose of this paper is to systematically compare and evaluate the performance of these cumulus parametrizations under summertime midlatitude continental conditions. Through this study, we hope to identify strengths and weaknesses of these cumulus parametrizations and hence eventually lead to further improvements by individual participating groups.

2. MODEL DESCRIPTIONS

Table 1 lists the 15 SCMs participating in the intercomparison study. Most of the SCMs are the same models that participated in the earlier case-study (Ghan *et al.* 2000) except for CCCma1_SP, ECMWF, GISS, MesoNH, MOUM and CCM3/SIO.

The parametrization schemes for deep and shallow/midlevel convection in these SCMs are listed in Table 2. It is seen that deep convection schemes used in some models

---

* Global Atmospheric Research Program (GARP) Atlantic Tropical Experiment.
† National Center for Atmospheric Research.

TABLE 1.   SUMMARY OF SCMS USED IN THE INTERCOMPARISON STUDY

Model (SCM)	Model full name	Reference(s)
CCCma	Canadian Center for Climate Modeling and Analysis, version 0	Lohmann *et al.* (1999)
CCCma1_SP	Canadian Center for Climate Modeling and Analysis, version 1	McFarlane *et al.* (1992); von Salzen and McFarlane (2002)
CCM3	NCAR Community Climate Model, version 3	Kiehl *et al.* (1996); Hack *et al.* (1998)
CCM3/SIO	Scripps Institution of Oceanography version of CCM3	Kiehl *et al.* (1996); Hack *et al.* (1998); Zhang (2002)
CCM3/SUNY	State University of New York version of CCM3	Kiehl *et al.* (1996); Hack *et al.* (1998); Xie and Zhang (2000)
CSIRO	Commonwealth Scientific and Industrial Research Organization Mark 3 (developmental)	Rotstayn (1997); Rotstayn *et al.* (2000)
CSU	Colorado State University	Randall and Cripe (1999)
ECMWF	European Centre for Medium-Range Weather Forecasts	Gregory *et al.* (2000) and Gregory (2001)
GFDL	NOAA Geophysical Fluid Dynamics Laboratory	See Ghan *et al.* (2000) for description of the GFDL model
GISS	NASA Goddard Institute for Space Studies	Del Genio and Yao (1993), and Del Genio *et al.* (1996)
McRAS	Microphysics of cloud/Relaxed Arakawa-Schubert scheme	Takacs *et al.* (1994); Sud and Walker (1999a,b)
MesoNH	Modele Mesoechelle Non-Hydrostatique	Lafore *et al.* (1998)
PNNL/CCM2	Pacific Northwest National Laboratory version of CCM2	Hack *et al.* (1993); Ghan *et al.* (1997)
Scripps	Scripps Institution of Oceanography	Iacobellis and Somerville (2000)
MOUM	Met Office Unified Model	Pope *et al.* (2000)

are very similar. For example, the schemes used in CCCma, CCCma1_SP, CCM3, CCM3/SIO, CCM3/SUNY and Scripps were originally proposed by Zhang and McFarlane (1995, henceforward ZM). GFDL and McRAS use a relaxed Arakawa–Schubert scheme (Arakawa and Schubert 1974, henceforward AS) that was originally proposed by Moorthi and Suarez (1992). And the bulk mass flux scheme proposed by Gregory and Rowntree (1990) is used in CSIRO and MOUM with some modifications.

All of the deep convection schemes are based on the mass flux approach, which uses either spectral cloud ensemble models similar to AS (e.g. CSU, GFDL and McRAS) or a bulk cloud ensemble model (e.g. CSIRO, ECMWF, GISS, MesoNH, PNNL/CCM2 and MOUM). In the bulk mass flux method, only one single cloud model is used to represent an average over all cloud types within a convective ensemble. Therefore, unlike the spectral method, the bulk method does not have explicit assumptions on the mass and thermodynamic budgets of sub-ensembles of cumulus clouds, and does not give explicit information on the mass spectrum of various cloud types. In addition, the entrainment and detrainment rates in the bulk method are often set to correctly estimate the maximum cloud-top height, while they are dependent on the spectral cloud distribution in the spectral method. Yanai *et al.* (1976) showed that these two types of methods gave nearly identical total vertical cloud mass flux for tropical convection.

It should be noted that the ZM scheme is different from the conventional bulk mass flux schemes. It is based on the same spectral rising plume concept as used in AS.

TABLE 2. SUMMARY OF DEEP AND SHALLOW/MIDLEVEL CONVECTION SCHEMES USED IN THE SCMs

Model	Deep convection scheme	Shallow/midlevel convection scheme
CCCma	Revised ZM (Lohmann, personal communication)	No
CCCma1_SP	Prognostic ZM (von Salzen, personal communication)	von Salzen and McFarlane (2002)
CCM3	ZM	Hack (1994)
CCM3/SIO	Revised ZM (Zhang 2002)	Same as CCM3
CCM3/SUNY	Revised ZM (Xie and Zhang 2000)	Same as CCM3
CSIRO	Bulk mass flux (Gregory and Rowntree 1990; Gregory 1995)	The deep convection scheme applicable to all types of convection
CSU	Prognostic AS (Ding and Randall 1998)	No
ECMWF	Bulk mass flux (Tiedtke 1989; Gregory et al. 2000; Gregory and Guichard, 2002)	Mass flux treatment but different closure/specification compared to deep convection
GFDL	Relaxed AS (Moorthi and Suarez 1992)	No
GISS	Bulk mass flux (DelGenio and Yao 1993)	The deep convection scheme applicable to all types of convection
McRAS	Revised relaxed AS (Sud and Walker 1993)	No
MesoNH	Bulk mass flux (Bechtold et al. 2001)	The deep convection scheme applicable to all types of convection
PNNL/CCM2	Bulk mass flux (Hack 1994)	The deep convection scheme applicable to all types of convection
Scripps	ZM	No
MOUM	Bulk mass flux (Gregory and Rowntree 1990; Gregory 1995)	The deep convection scheme applicable to all types of convection

ZM is Zhang and McFarlane (1995).
AS is Arakawa and Schubert (1974).

The bulk entrainment rate as a function of height is the same as a spectral model would produce because the same spectral concept is used to estimate it. However, by assuming a constant spectral distribution in cloud-base mass flux, the thermodynamic equations are reduced to the bulk form. The ZM scheme is designed primarily to treat deep convection, therefore some models use an additional scheme for shallow and mid-level convection. In contrast, the conventional bulk mass flux schemes are designed to represent shallow, mid-level and deep convection as functions of the cloud depth and the starting level.

Other important features of these cumulus parametrizations are summarized in Table 3, such as closure assumptions, triggering mechanisms and convective down-draughts. Most models use a closure based on the assumption that CAPE is consumed by cumulus convection over a given time-scale (CAPE closure). The time-scale is usually set to be a few hours. CCM3/SIO revises the CAPE closure for the ZM scheme so that the cloud-base mass flux is determined by the CAPE generation rate due to the large-scale tropospheric forcing (Zhang 2002). CSU employs a prognostic closure using the cumulus kinetic energy (Pan and Randall 1998) for the AS scheme. CCCma1_SP uses a similar prognostic closure suggested by Pan and Randall (1998) to account for the effects of self-organization of convective systems for the ZM scheme (von Salzen 2001, personal communication). Some of the bulk mass flux schemes use a closure based on a stability-dependent mass flux (i.e. CSIRO, GISS and PNNL/CCM2).

TABLE 3.   SUMMARY OF SOME RELEVANT ASPECTS OF THE DEEP CONVECTION SCHEMES

Model	Closure	Triggering mechanism	Downdraughts
CCCma	CAPE	CAPE > 0 and buoyancy at LCL > 0.1 K	Convective precipitation induced downdraughts. Downdraughts starting at or below the updraught detrainment layer. No downdraughts below cloud base
CCCma1_SP	Prognostic closure	CAPE > 0	Same as CCCma
CCM3	CAPE	CAPE > 0	Same as CCCma
CCM3/SIO	CAPE generation rate	CAPE generation rate > 0	Same as CCCma
CCM3/SUNY	CAPE	Positive dynamic CAPE	Same as CCCma
CSIRO	A stability-dependent mass flux	Parcel buoyancy	Downdraughts exist if the updraught is saturated and the depth of cloud layer exceeds 150 hPa. Downdraughts not allowed within 100 hPa of the surface
CSU	A prognostic closure using the cumulus kinetic energy	CWF > 0 and constraints on the entrainment rate and the saturation of cloudy air at the cloud top	No
ECMWF	CAPE	Parcel buoyancy	Convective precipitation induced downdraughts.
GFDL	Relax the state toward quasi-equilibrium	CWF > 1.4 ∗ CWF$_{clim}$ for a given updraught type	No
GISS	Cloud base neutral buoyancy	Parcel buoyancy	Downdraughts specified to be a third of updraughts
McRAS	Same as GFDL	CWF > 0 and RH > RH$_{crit}$	Rain-evaporation induced downdraughts
MesoNH	CAPE	Parcel buoyancy and vertical motion	Convective precipitation induced downdraughts
PNNL/CCM2	A stability-dependent mass flux	Parcel buoyancy	No
Scripps	CAPE	CAPE > 0	Same as CCCma
MOUM	CAPE	Parcel buoyancy	Similar to CSIRO

CWF is the cloud work function defined by Arakawa and Schubert (1974); CWF$_{clim}$ is the climatological value of CWF given in Lord and Arakawa (1980); CAPE is convective available potential energy; LCL is the lifting condensation level.

The primary triggering mechanisms used in these cumulus parametrizations are either based on CAPE (or CWF*), or based on local parcel buoyancy. The former measures the instability based on the vertical integral of parcel buoyant energy, while the latter measures the instability by lifting a parcel through a specific distance or between two model layers. Most schemes with the CAPE/CWF triggers need additional constraints as shown in Table 3. For example, CCM3/SUNY requires a positive contribution from large-scale dynamic processes to the existing positive CAPE (Xie and Zhang 2000). McRAS uses the relative humidity (RH) that exceeds 0.9 times the critical value, RH$_{crit}$, for stratiform condensation, in addition to the positive CWF.

* The cloud work function (CWF) as defined by Arakawa and Schubert (1974) is a function of cloud types and is equal to CAPE when the entrainment rate is zero.

Another feature seen from Table 3 is that convective-scale precipitation-driven downdraughts are parametrized in most of the models except for PNNL/CCM2, CSU and GFDL. In addition, almost all models treat convection as penetrative convection except for PNNL/CCM2 which uses a convection scheme that is based on a three-level non-entraining cloud model (Hack 1994).

There are also many differences among the SCMs in parametrizing physical processes such as stratiform cloud formation, radiation and turbulent processes. For example, most models use a prognostic scheme to predict stratiform cloud condensate, except for CCCma1_SP, CCM3, CCM3/SIO and CCM3/SUNY which use a diagnostic scheme to estimate cloud fraction and cloud condensate. Some models (CSU, ECMWF, GFDL, GISS, McRAS, MesoNH, PNNL/CCM2 and Scripps) consider the detrainment of condensate water from cumulus clouds in their prognostic cloud scheme. Radiation schemes in most models are from either the ECMWF model or the NCAR CCM. They employ a variety of turbulent parametrization schemes. Detailed descriptions of these schemes can be found in the references listed in Table 1.

3. DATA

The data used to drive and evaluate the SCMs and CRMs were collected at the ARM SGP site during the summer 1997 IOP, from 18 June (2330 UTC, Julian day 170) to 17 July (2330 UTC, Julian day 199; hereafter Day is used instead of Julian day). Observations at the ARM site used to characterize the atmospheric column include: three-hourly soundings at five locations, surface data from the meteorological network, wind profiler data, satellite data and radar rainfall estimates; details are given in Ghan *et al.* (2000). The horizontal and vertical advective tendencies of temperature and moisture and vertical velocity are derived from the constrained variational analysis (Zhang and Lin 1997; Zhang *et al.* 2001). In the analysis, the atmospheric state variables are forced to satisfy the conservation of mass, heat, moisture and momentum. Ghan *et al.* (2000) showed that the variational analysis approach significantly improved the quality of the input data, and thereby the SCM simulations.

The summer 1997 IOP contained a wide range of summertime weather conditions. The ARM SGP site experienced several intensive precipitation events and dry and clear days during this IOP (Fig. 1), associated with the activities of the large-scale upper-level troughs and ridges over the North American continent. The three subperiods defined by A, B and C in Fig. 1, with each including two or three precipitation events and lasting for 4 or 5 days, were selected to test model performance. To help illustrate the synoptic conditions during the three subperiods, Fig. 2 shows a series of 4 km resolution infrared cloud images, corresponding to the peaks of the eight strong precipitation events that occurred on Days 179, 180–181, 190, 191, 192, 195, 196 and 197–198, from the seventh NOAA GOES* (GOES-7) measurements. The circle in Fig. 2 is the variational analysis domain or the SCM domain.

Subcase A features a weak precipitation event that occurred on Day 179 and a strong precipitation event on Days 180–181. The weak precipitation event was associated with very moist air along with the tail end of a front moving eastward across the SGP site. Several localized individual thunderstorms developed in early morning in the southern part of the SCM domain. However, the domain-averaged precipitation was very weak. The heavy precipitation event on Days 180–181 was mainly associated with a complex of thunderstorms that developed in south-eastern Kansas in the late evening of Day 180

* National Oceanic and Atmospheric Administration Geostationary Operational Environmental Satellite.
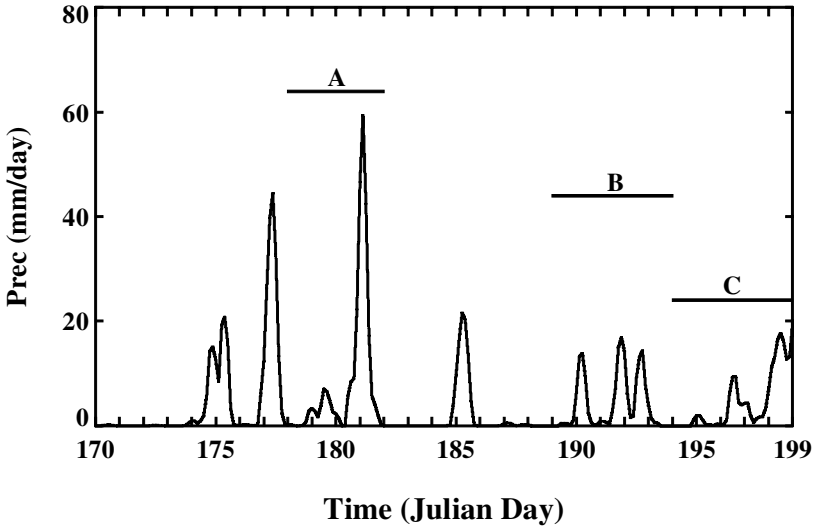
Figure 1. Time series of the observed surface precipitation rates during the summer 1997 Intensive Observing Period. Labels A, B and C show the three subcases selected in the study.

local time (here local noon corresponds to 1700 UTC) and moved south-eastward across the SCM domain during Days 180–181. The strong convective complex affected the major parts of the SCM domain. This convective event was well captured by the ARM sounding array.

Subcase B contained three precipitation events. The first one (Day 190) was related to a complex of thunderstorms that developed in south-eastern Kansas during the evening of Day 190 and moved south-eastward into south-western Missouri and north-eastern Oklahoma overnight. Only the northern edge of the ARM sounding array experienced heavy rainfall judging from the Arkansan Basin Red River Forecast Center (ABRFC) 4 km WSR-88D radar precipitation estimates (not shown). The other two precipitation events (Days 191 and 192) were more localized. They were associated with a developing upper-level trough that extended south-eastward over the North American continent. The southern edge of the trough moved across the SCM domain and brought in a moist and unstable air mass to the area. The large-scale circulation and diurnal heating allowed isolated/scattered showers and thunderstorms to develop within the SCM domain in late afternoon and evening during Days 191 and 192.

Subcase C experienced one very weak precipitation event on Day 195 and two consecutive precipitation events over the last three days. The weak precipitation event was associated with isolated thunderstorms along with a slow moving cold front. The convective system developed within the SCM domain, however, it only occupied a small part of the SCM domain; most of the SCM domain was clear. The second precipitation event on Day 196 was associated with a trough of low pressure moving eastward into the SGP site. A complex of thunderstorms started to develop early in the morning of Day 196 in the north-western part of the SCM domain and then slowly moved over the entire domain. The third precipitation event was associated with a nearly stationary upper-level trough that developed and extended south-eastward across the SGP site. Thunderstorms developed during the evening between Wichita, Kansas and Ponca City,
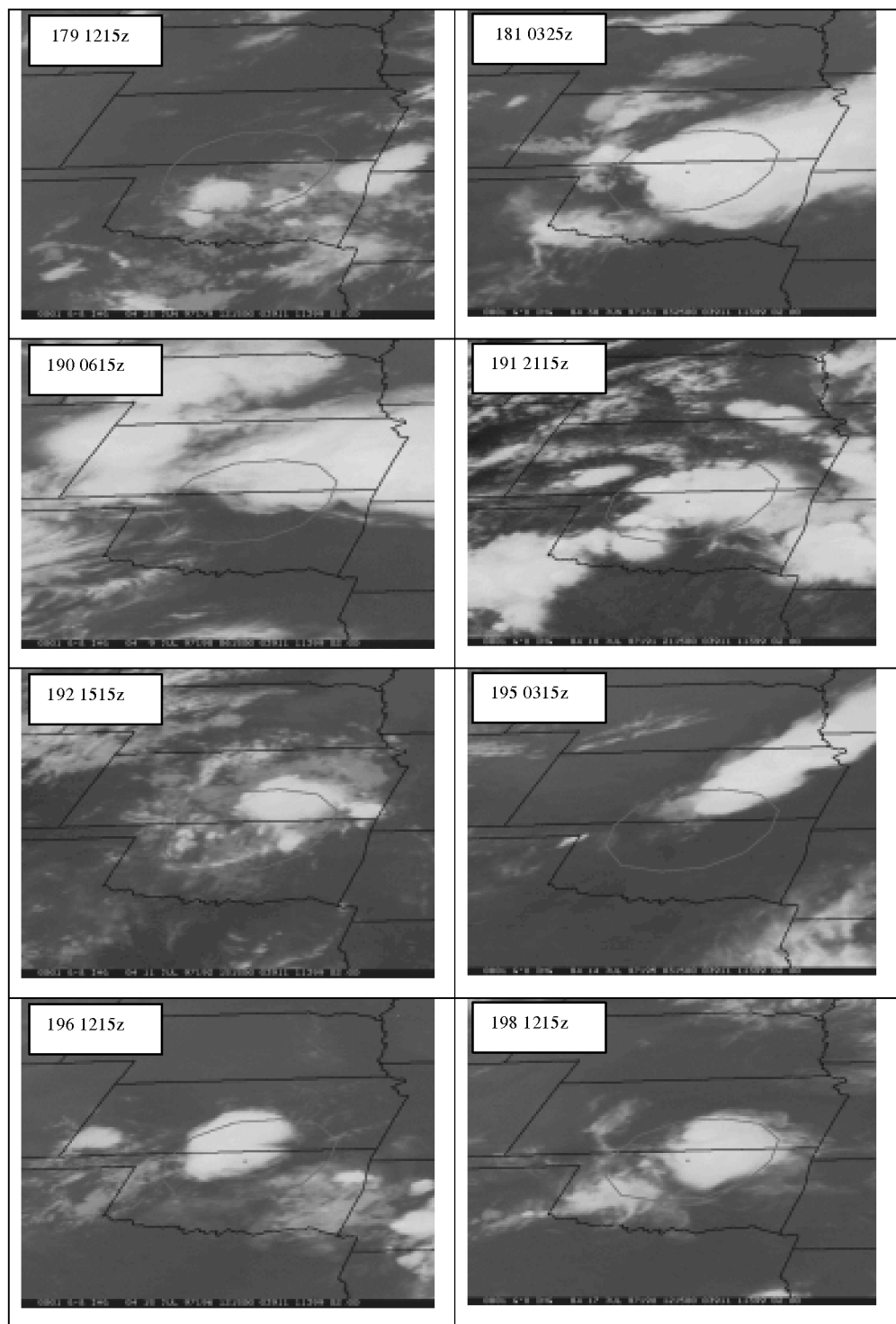
Figure 2. Satellite infrared cloud images corresponding to the peaks of the eight strong precipitation events that occurred on Julian days 179, 180–181, 190, 191, 192, 195, 196 and 197–198 during the summer 1997 Intensive Observing Period.
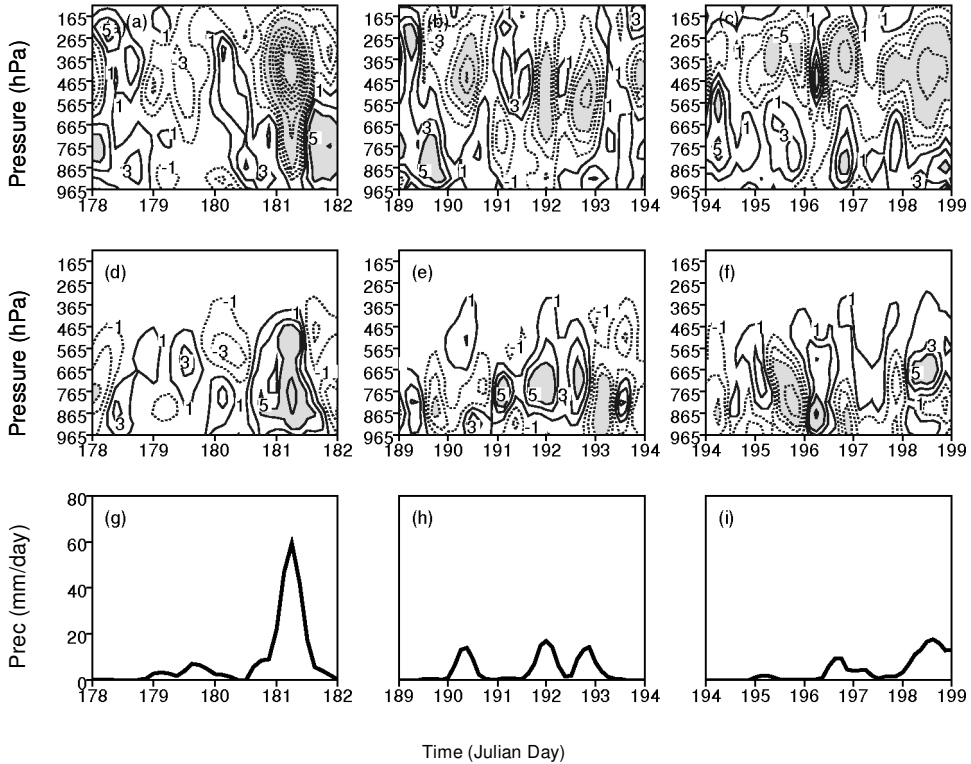
Figure 3.   Time–height cross-sections of observed large-scale advective tendencies of: (a), (b) and (c) temperature (K day^{-1}) for Subcases A, B and C, respectively; (d), (e) and (f) similar but for moisture (g kg^{-1}day^{-1}); (g), (h) and (i) similar but for surface precipitation rates (mm day^{-1}). In (a) to (f) contour values are -35, -30, -25, -20, -15, -10, -5, -3, -1, 1, 3, 5, 10, 15, with areas greater than 5 or less than -5 shaded, and negative contours dotted.

Oklahoma and it continued to rain over the same general area for about 12 hours. The north-eastern part of the domain experienced heavy rainfall.

As described above, for the eight precipitation events of the three subcases some of the convective events were located well within the SCM domain and some were not. For the latter cases, the SGP sounding array may not properly capture the characteristics of the strong convective complex.

4.   INTERCOMPARISON AND INTERPRETATION OF SIMULATION RESULTS FROM THE BASELINE EXPERIMENT

The baseline experiment in this study uses the horizontal and vertical advective tendencies of temperature, moisture and surface fluxes specified from the observations, and the radiative heating rates are calculated from model parametrizations; see Cederwall *et al*. (2000) for a detailed description of experiment design. Figure 3 shows the total large-scale advective tendencies of temperature and moisture, and the corresponding surface precipitation rates for Subcases A, B and C. It is seen that the forcing is very strong during the strong precipitation event that occurred on Day 181 in Subcase A, and it is relatively weak during other precipitation periods. In general, the observed precipitation events correspond to the large-scale advective cooling in the middle and upper troposphere (maximum centred at 400–450 hPa) and moistening in the lower

TABLE 4.   TIME-MEAN SURFACE PRECIPITATION
RATES (mm DAY^{-1})

Convective events (Julian days)	Total	Cumulus	Stratiform
179 (A)	4.14	2.17	1.97
180–181 (A)	24.7	20.1	4.6
190 (B)	9.33	7.20	2.13
191 (B)	10.54	7.13	3.41
192 (B)	7.27	3.61	3.76
195 (C)	1.96	1.56	0.40
196–197 (C)	6.30	4.97	1.33
197–198 (C)	10.0	6.92	3.07
Total mean	9.28	6.70	2.58

Letters A, B and C in parenthesis denote Subcases A, B and C.

troposphere (maximum centred at about 750 hPa); however, for the first precipitation events in Subcases B and C, the upper-level advective cooling is actually associated with weak low-level moisture divergence. Recall that only small portions of the SCM domain experienced precipitation during these two precipitation events. This suggests that the domain-averaged large-scale forcing may not be able to properly capture the typical thermodynamic structure of a strong convective complex.

(a)   Surface precipitation rates

Surface precipitation rates are closely related to model cumulus convection schemes, therefore they are evaluated first. The satellite images clearly show that the precipitation events during these subperiods were associated with mesoscale convective systems that were influenced by the large-scale circulations. To quantitatively demonstrate the relative importance of cumulus clouds and stratiform clouds in these convective events, we partitioned the total rainfall into convective and stratiform components based on the ABRFC 4 km radar data using the algorithm developed by Johnson and Hamilton (1988). They used 6 mm h^{-1} as the threshold for convective–stratiform partitioning of an OK PRE-STORM* squall line.

Most of the convective events are dominated by cumulus precipitation, especially in the case of the strong precipitation event that occurs on Days 180–181, in which more than 80% of surface rainfall is from cumulus clouds (Table 4). The exceptions are the first precipitation event in Subcase A and the third precipitation event in Subcase B, in which cumulus clouds and stratiform clouds have comparable contributions to the total precipitation. For all three subperiods combined, 72% of surface rainfall is from cumulus clouds, but 28% are from stratiform clouds.

Figures 4(a)–(f) show time series of the total and stratiform precipitation rates estimated from the radar data (black line) and simulated from 13 SCMs for Subcases A, B and C. Note that results from CCM3/SIO and CCM3/SUNY are not shown in the baseline experiment. Because these two models are identical to CCM3 except for some details of cumulus parametrizations, their results will be shown in section 5 to illustrate the sensitivity of CCM3 simulations to different convective triggering mechanisms and closure assumptions.

It is seen that most models simulate reasonably well the strong precipitation event (Days 180–181) in Subcase A and the last two precipitation events (Days 191–192) in

* Oklahoma-Kansas Preliminary Regional Experiment for STormscale Operational and Research Meteorology.
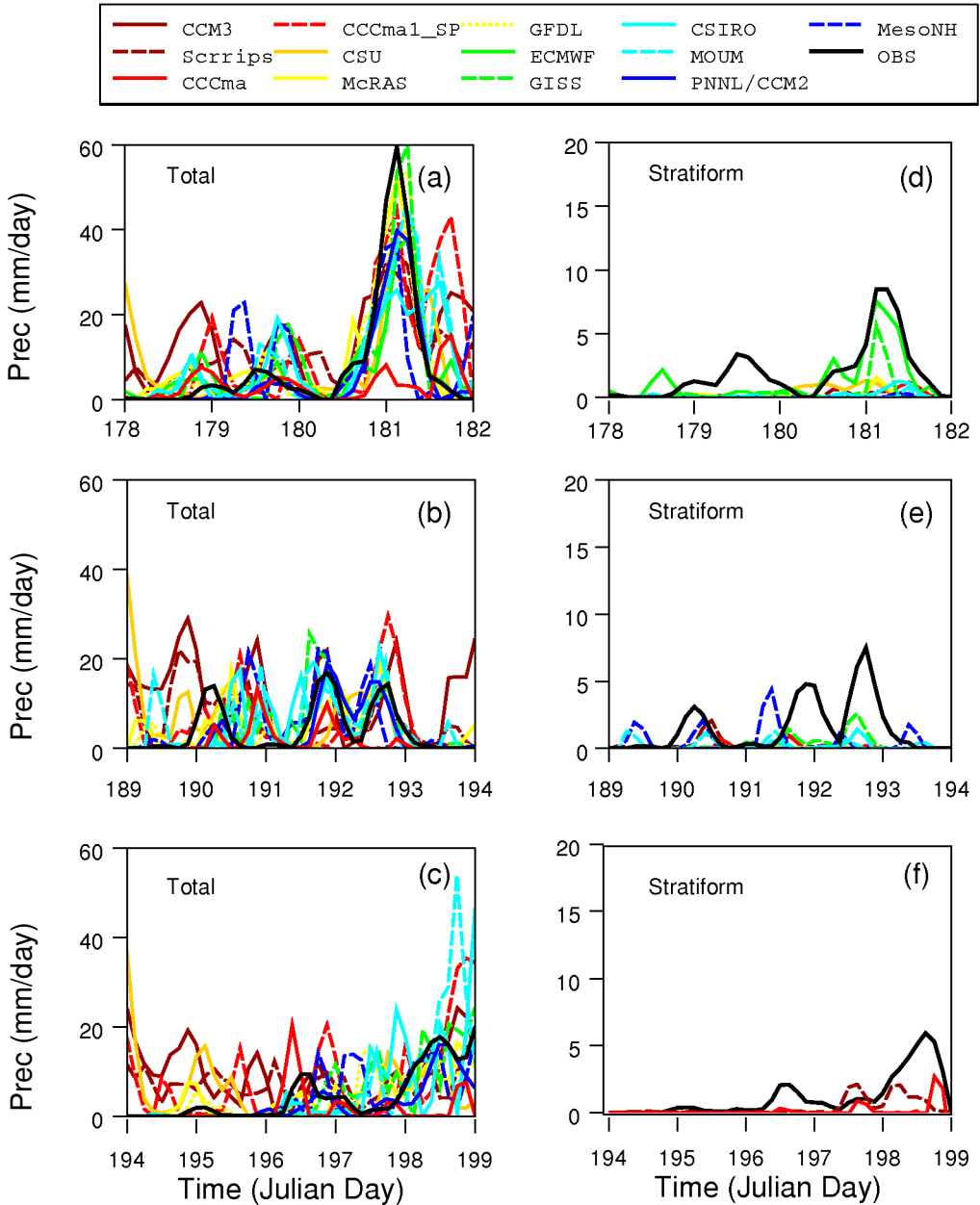
Figure 4.   Time series of observed (black line) and simulated rates of: (a), (b) and (c) total surface precipitation for Subcases A, B and C, respectively; (d), (e) and (f) similar but for stratiform surface precipitation. Models shown in the key are discussed in the text.

TABLE 5. TIME-MEAN TOTAL PRECIPITATION RATES
(mm DAY^{-1}) DURING SUBPERIODS A, B AND C

Models	Subcase A	Subcase B	Subcase C
Observation	8.21	4.17	4.72
CCM3	13.18	10.88	9.28
Scripps	10.83	6.98	7.09
CCCma	3.25	1.62	1.69
CCCma1_SP	11.76	5.93	6.92
CSU	8.78	6.05	5.56
McRAS	9.10	4.76	4.45
GFDL	8.79	4.92	4.38
ECMWF	6.88	N/A	3.05
GISS	8.37	5.07	4.56
CSIRO	8.41	4.91	4.00
MOUM	8.92	5.00	5.54
PNNL/CCM2	5.63	3.23	2.86
MesoNH	6.98	6.1	4.71

Subcase B, though they are less successful in simulating the rest of the convective events (Figs. 4(a)–(c)). A noticeable feature appearing in Figs. 4(a)–(c) is that some models show large spurious precipitation during non-precipitation periods. This is especially true for the models that use positive CAPE only as a triggering mechanism (see Table 3), such as CCM3, Scripps and CCCma1_SP. They produce pronounced diurnal variations of surface precipitation that are not observed. This is less serious in those models with triggering mechanisms based on CAPE/CWF with additional constraints or the parcel buoyancy methods, except for CSU in which convection is occasionally too active. It is also noticed that CCCma largely underestimates most of the precipitation events. This suggests that the revised triggering mechanism for ZM used in CCCma overly inhibits convection. PNNL/CCM2 also underestimates the magnitudes of most of the precipitation events except for the last two events in Subcase B.

Figures 4(d)–(f) show that stratiform precipitation rates are greatly underestimated in all SCMs. For most of the convective events little stratiform precipitation is produced in most models. Only ECMWF and GISS produce reasonable stratiform precipitation amounts during the strong precipitation event in Subcase A. This is partly because cumulus convection is too active in most models, and cumulus convection consumes most of the moisture transported from the boundary layer. Assumptions on detrainment of condensate water from cumulus clouds could also contribute to this problem.

Table 5 shows the time-averaged total precipitation rates for Subcases A, B and C. Consistent with the discussion above, CCM3, Scripps, CCCma1_SP, MesoNH (Subcase B only) and CSU (Subcase B only) greatly overestimate the observed surface precipitation rates, while CCCma, ECMWF, MesoNH (Subcase A only) and PNNL/CCM2 greatly underestimate the observed values of all subperiods. The rest of the models have time-averaged precipitation rates within 1 mm day^{-1} of the observations.

To quantify the statistical similarity among the models, Figs. 5(a) and (b) present a Taylor diagram (Taylor 2001) for the total and convective surface precipitation fields, respectively. In Fig. 5, points A1 to A3 represent the models that use CAPE-only triggers, points B1 to B4 represent the models that use CAPE/CWF triggers with additional constraints, points C1 to C5 represent the models that use the parcel buoyancy triggers, point X represents the consensus of ten CRMs results (Xu *et al.* 2002), and point Obs represents the observations. Note that a CRM consensus for convective precipitation is not shown because only a few models provide the data. For simplicity,
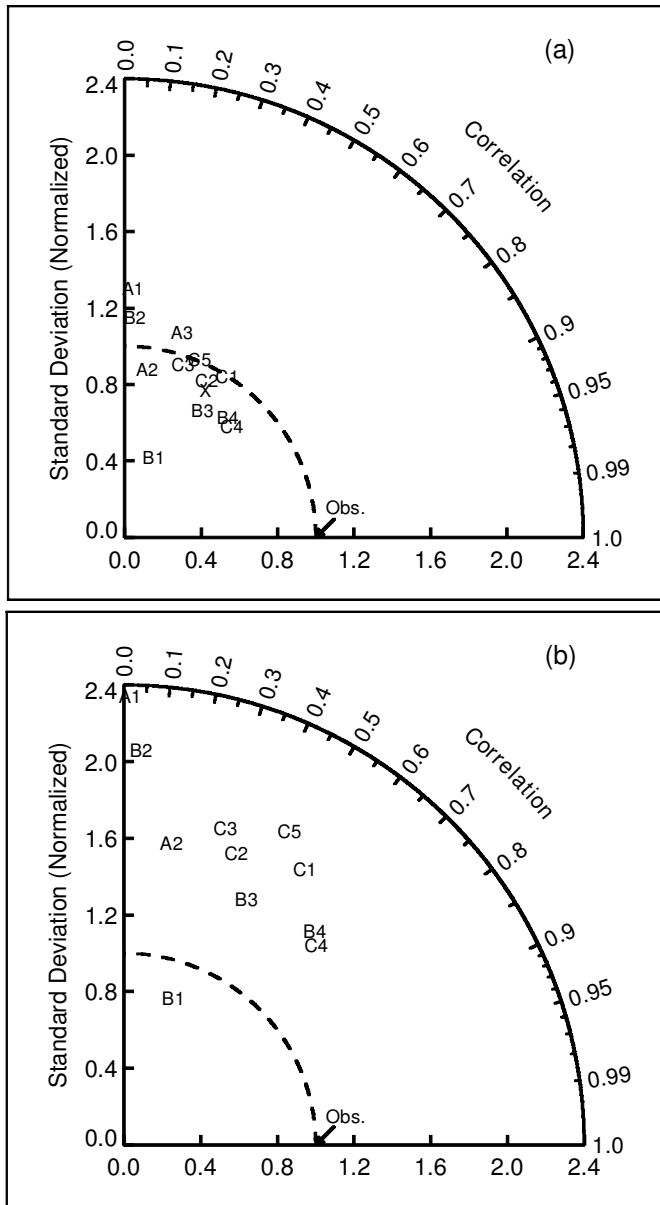
Figure 5.   A Taylor diagram showing how closely the simulated surface precipitation rates match observed values for: (a) total precipitation rate, and (b) convective precipitation rate, both for Subcase B. This polar style graph is designed to show the correlation coefficient for a field between observations and simulations (azimuthal position), the standard deviation of observed and simulated fields (radial distances), and the RMS errors once any overall bias has been removed (the distance connecting the observation and simulation points). Note that the RMS error and the standard deviation are normalized by the standard deviation of the corresponding observed field. The standard deviation of the observed field is normalized by itself and it must, therefore, always be plotted at unit distance from the origin along the abscissa. Labelled points represent RMS errors for different models: A1 denotes CCM3, A2 Scripps, A3 CCCma1_SP, B1 CCCma, B2 CSU, B3 McRAS, B4 GFDL, C1 GISS, C2 CSIRO, C3 MOUM, C4 PNNL/CCM2, C5 MesoNH, X the consensus of ten CRMs, and Obs observations. See text for details of the models.

here we only show results for Subcase B. Results from Subcase A for most models except CCCma show much better agreement with the observations than those from Subcase B, because Subcase A is characterized by a strong precipitation event associated with a strong large-scale forcing (Figs. 3(a), (d) and (g)) and most schemes could simulate the convection well in such environments. Results from Subcase C are similar to Subcase B.

Comparing Figs. 5(a) and (b), almost all models except CCCma (B1) show better agreement with the observations for the total precipitation field than for its convective part in terms of the RMS error and the amplitude of temporal variability, while the correlation coefficients are similar for both fields. Another feature is that most models except CCCma overestimate the observed temporal variations in the convective precipitation field. This is consistent with the fact that most models overestimate the convective precipitation and underestimate the stratiform precipitation, as discussed earlier.

In general, the models that use the CAPE-only triggers and CSU (point B2) produce the least agreement with the observations. The rest of the models generally produce comparable results to the CRM consensus (point X). Note that the CRMs have much smaller inter-model differences in the surface precipitation field than those seen in the SCMs and the first precipitation event is severely delayed in Subcase B (Xu *et al*. 2002). The comparable results suggest that these SCMs are doing as well as can be expected given uncertainties in the forcing and the observed rainfall.

It is also noteworthy that the correlation coefficients in these models, except GFDL (B4) and PNNL/CCM2 (C4), are also quite small (less than 0.6). The small coefficients are partly due to the failure by these SCMs to promptly initiate the first convective event of Subcase B (Fig. 4(b)). This is also the case in all CRM simulations (Xu *et al.* 2002). The delayed convection may be caused by the dry thermodynamic profiles at the beginning of the event as discussed below.

Both SCMs and CRMs are driven by the area-averaged large-scale forcing. In some instances, however, the forcing may not be representative of those convective events that are only partly located within the SCM domain, such as the first precipitation events of the three subcases (Fig. 2). Figures 6(a)–(d), respectively, show the vertical profiles of moist static energy (MSE, solid line) and saturated MSE (dashed line) at the beginnings of four selected precipitation events that occurred on Days 180–181, 190, 191 and 195 of Subcases A, B and C, together with the sounding profiles at the station where convection is occurring. Figures 6(e)–(h), are the same as Figs 6(a)–(d) except that they are calculated from the SCM domain average profiles. The MSE values are normalized by C_{pd} ($1004 \, \mathrm{J \, kg^{-1} K^{-1}}$), the specific heat at constant pressure. Comparing Figs. 6(a)–(d) with Figs. 6(e)–(h), it is much easier to diagnose convection from the single-sounding profiles than from the SCM domain-averaged profiles. Another noticeable feature is that sometimes convection is triggered at higher levels (e.g. probably Day 191, Figs. 6(c) and (g)) and some models may not handle that well.

Figure 6 also helps us to understand why most models perform well for some convective events and worse for the others. We have shown in Fig. 4 that most models typically performed well for the convective events that occurred on Days 180–181 in Subcase A and Days 191–192 in Subcase B. Recall that these convective events were well developed within the ARM SCM domain and most parts of the domain experienced rainfall. Thus, the mean thermodynamic profiles can properly describe the characteristics of convective systems. As shown in Figs. 6(e) and (g), which correspond to these convective events, the domain-averaged thermodynamic profiles show that the environmental atmospheres are conditionally unstable and there is enough moisture at low levels to make a parcel lifted a reasonable distance buoyant. In contrast, for the
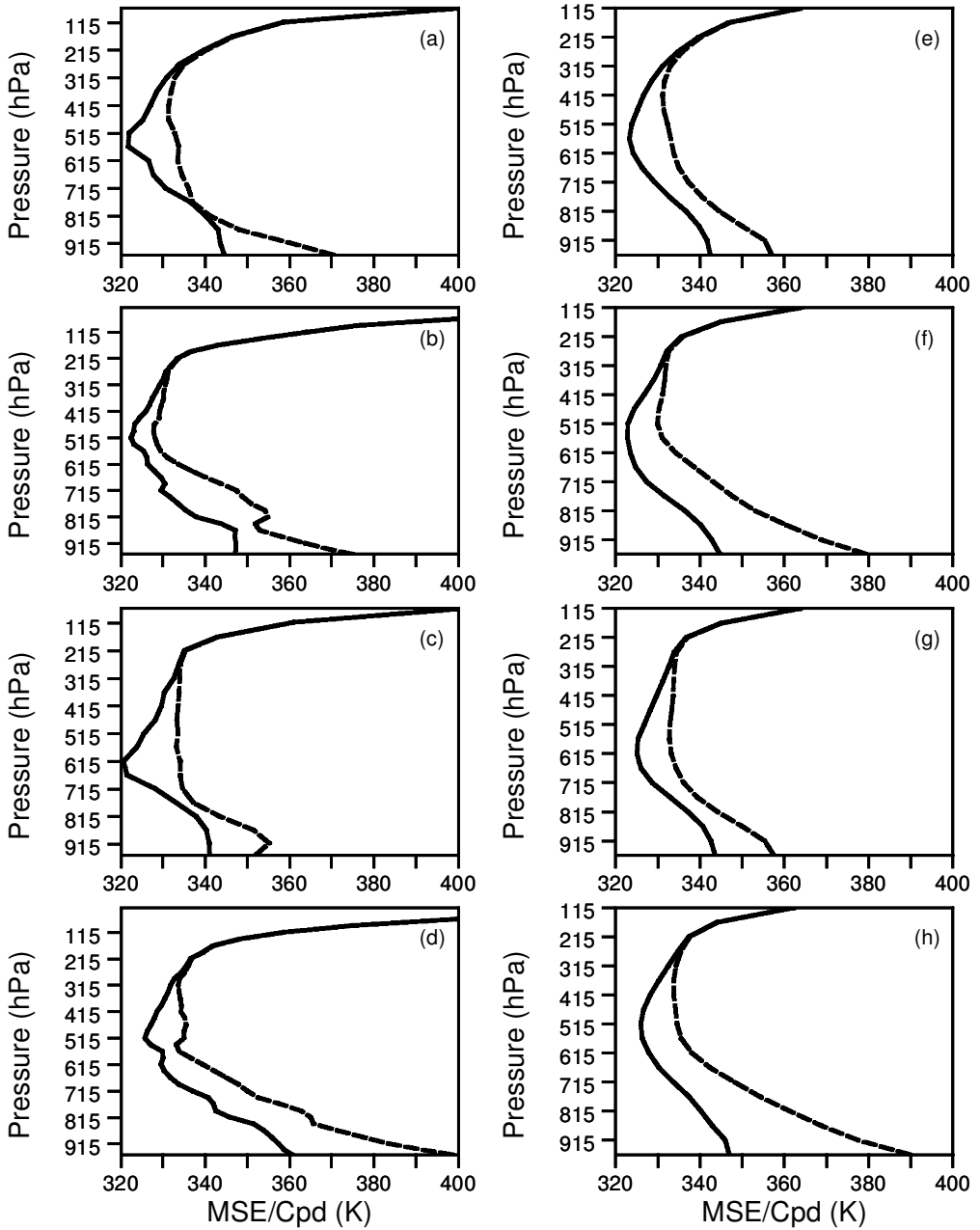
Figure 6. Vertical profiles of moist static energy (MSE, solid) and saturated MSE (dashed) corresponding to the beginnings of four selected precipitation events. (a) Days 180–181, (b) Day 190, (c) Day 191, and (d) Day 195, all with MSE calculated from the sounding profiles at the station where convection is occurring; (e), (f), (g) and (h) are similar but with the MSE calculated from the ARM SCM domain (see text) mean soundings.
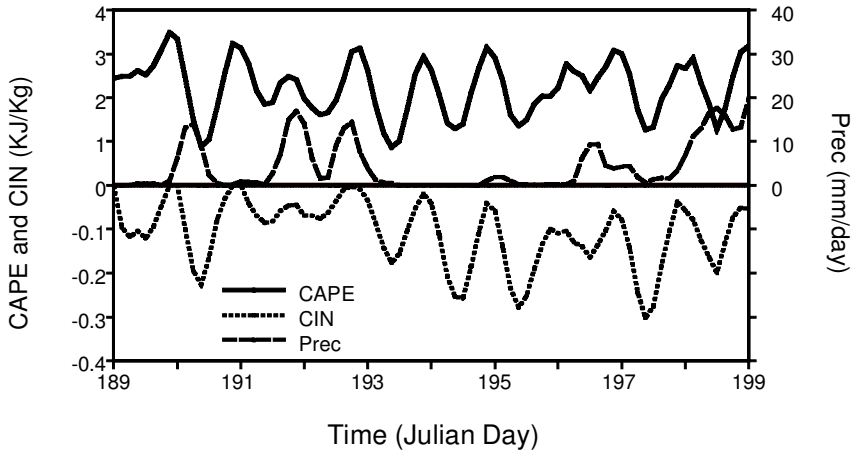
Figure 7. Time series of convective available potential energy (CAPE), convective inhibition (CIN), and precipitation for the last ten days of the summer 1997 Intensive Observing Period, which covers the period of Subcases B and C.

convective cases in which only a part of the domain was affected by convective systems, such as the first precipitation events of Subcases B and C, the average profiles (Figs. 6(f) and (h)) are so dry at low levels that few cumulus parametrizations would be triggered. This indicates that the problem with trying to validate SCMs against the timing of specific convective events is that, without knowledge of the probability distribution functions (pdfs) of temperature and moisture in the planetary boundary layer (PBL), it is impossible to tell whether a profile that is not overly conducive to convection in the mean has a tail of the distribution within the gridbox that *is* conducive. It suggests a need to use CRMs to develop pdfs of PBL properties that might give developers of SCMs insights into how to get the statistics of convective occurrence right.

The aforementioned discussions on the timing of simulated precipitation also suggest that deficiencies in convective triggering mechanisms are responsible for the precipitation errors in some models, such as CCM3, Scripps, CCCMa1_SP, CSU and CCCma. It is also noted that the triggering mechanisms used in these models are all primarily based on CAPE/CWF. The surface sensible- and latent-heat fluxes can greatly affect the generation of CAPE over the land surface where these fluxes are large and have strong diurnal variations. Over these areas convection could be more active for schemes using CAPE/CWF than for those using parcel buoyancy as triggering mechanisms if no additional constraint is used.

To help in discussing this issue, we analyse CAPE and CIN (convective inhibition) based on the ARM observations for Subcases B and C (Fig. 7). The observed surface precipitation rates are also shown. CAPE is calculated under the assumption that an air parcel ascends along a reversible moist adiabat with the originating level at the surface. CIN is the negative value of CAPE between the free convection level and the surface.

It is seen that CAPE exhibits strong diurnal variation, with its maximum during daytime and minimum during night-time due to the strong solar diurnal cycle over the land surface. The opposite is true for CIN which is usually large during non-precipitating periods. A large CIN value prevents convection from consuming the large amount of CAPE existing during these periods. Therefore, a positive CAPE is not a sufficient condition to trigger convection. In fact, there are obvious phase shifts between the observed CAPE and surface precipitation rates since most of the convective events occur

in late evening and early morning. Therefore, it is not surprising to see the excessive initiation of convection in those models that use only the CAPE trigger to diagnose the onset of convection. It should be noted that the triggering problem over tropical oceans might not be as serious as over the midlatitude land, since the diurnal variation of CAPE is weak over the sea due to weak diurnal fluctuations of surface fluxes.

(b)   Cloud fractions and outgoing long-wave radiation fluxes

Because all SCMs include cloud parametrizations, in addition to cumulus para-metrizations, it is necessary to show how the clouds and radiation are impacted by some of the deficiencies in cumulus parametrizations discussed earlier. Like Fig. 5, Fig. 8(a) presents a Taylor diagram for column cloud fractions of Subcase B among the SCMs. Note that cloud fraction data are not available for CSU (point B2). The observed cloud fraction is from the retrievals of ground-based millimetre wave cloud radar (Moran *et al.* 1998) at the ARM central facility. Time series of the observations are shown in Xu *et al.* (2002), which indicate rather large temporal variations for this subcase.

Most SCMs show large variabilities, as in the observations, except for CCM3 (point A1) and CCCma1_SP (point A3) which produce nearly overcast conditions at most times. As mentioned earlier, no prognostic cloud parametrization is implemented in these two models. Another noticeable feature shown in Fig. 8(a) is that there are large differences among the models even where they use similar cumulus parametrizations. This implies that the details in the cloud parametrizations impact the simulations of cloud fraction. Compared to the consensus of CRM results, the SCMs generally show better simulations in the amplitude of the temporal variability, but RMS errors are larger and the correlations with the observations are mostly lower.

The observed outgoing long-wave radiative fluxes (OLR) at the top of the atmos-phere (TOA) from GOES satellite observations are compared with simulations in Fig. 8(b) also for Subcase B. Note that CRM results are not available because of the pre-scribed radiation in their simulations. It is seen that most models exaggerate the ampli-tude of the temporal variability compared with that observed, but CCM3 (point A1) and Scripps (point A2) underestimate the temporal variability. Differences in OLR among the SCMs are mainly in the amplitude of the temporal variabilities, compared to surface precipitation rates and column cloud fractions (Fig. 5 and Fig. 8(a)). This suggests that the impact of convection and stratiform cloud on the radiative energy is significant in the context of the SCM modelling approach.

(c)   Temperature and moisture structures

The simulated temperature and moisture biases (Fig. 9) are averaged between pressure levels 115–915 hPa to minimize their being influenced by PBL processes. A noticeable feature seen in Fig. 9 is that the model simulations start to diverge after a few hours of integration. The models with excessive precipitation, such as CCM3, Scripps and CSU (Subcases B and C only), generally produce larger warm/dry biases. The excessive convective activities result in more convective heating and drying. CCCma also shows rather large warm/dry biases during most of the periods even though the model largely underestimates the observed convective events; the reason is unclear and needs to be investigated further. On the other hand, PNNL/CCM2 shows rather large cold and moist biases; this is mainly related to the non-penetrative convection scheme used in the model. As shown later, a non-penetrative convection scheme greatly underestimates the depth of instability and therefore leads to large cold and moist biases. For other models, temperature and moisture biases are relatively small for the layer means.
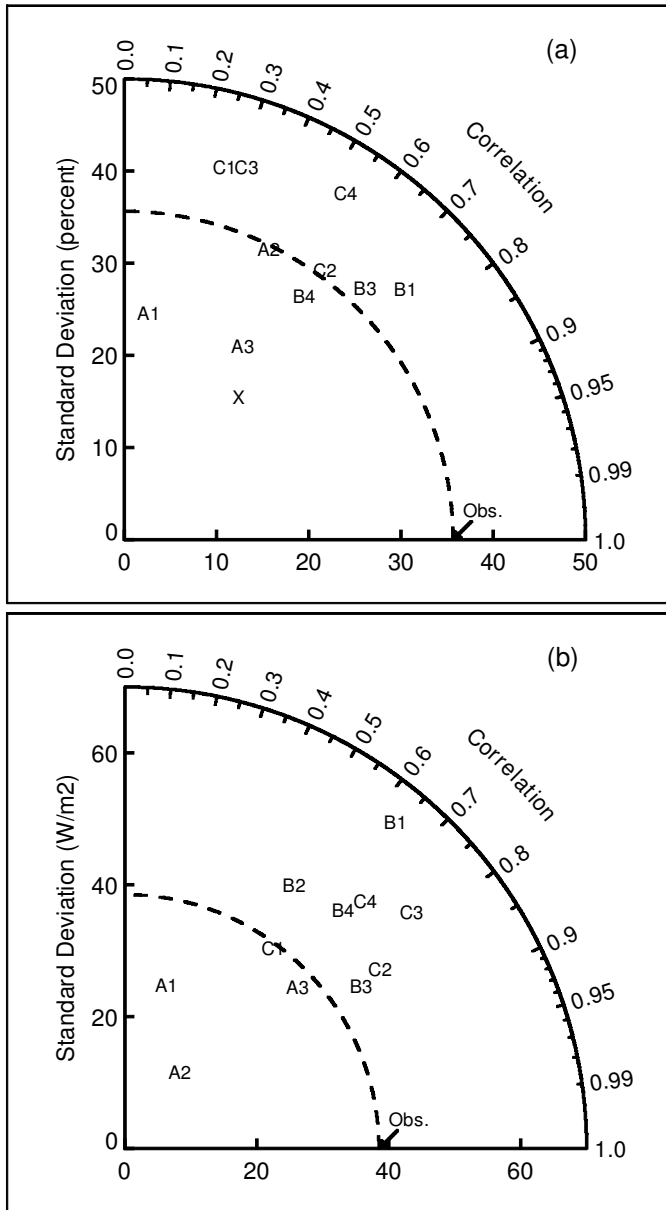
Figure 8.   Same as Fig. 5 but for: (a) column cloud fractions, and (b) top of atmosphere outgoing long-wave radiation fluxes, and in these the standard deviations are not normalized.

Next, the vertical structures of the temperature and moisture departures from observations, averaged over the three sub-periods, are shown in Fig. 10. For temperature (Figs. 10(a)–(c)), most SCMs generally produce smaller errors in the middle troposphere and slightly larger errors in the lower and upper troposphere. The exceptions are CCM3 and Scripps, which show large warm biases throughout the troposphere. In the upper troposphere, the models with the ZM and AS types of convection schemes generally produce warmer atmospheres than those with the conventional bulk mass flux schemes
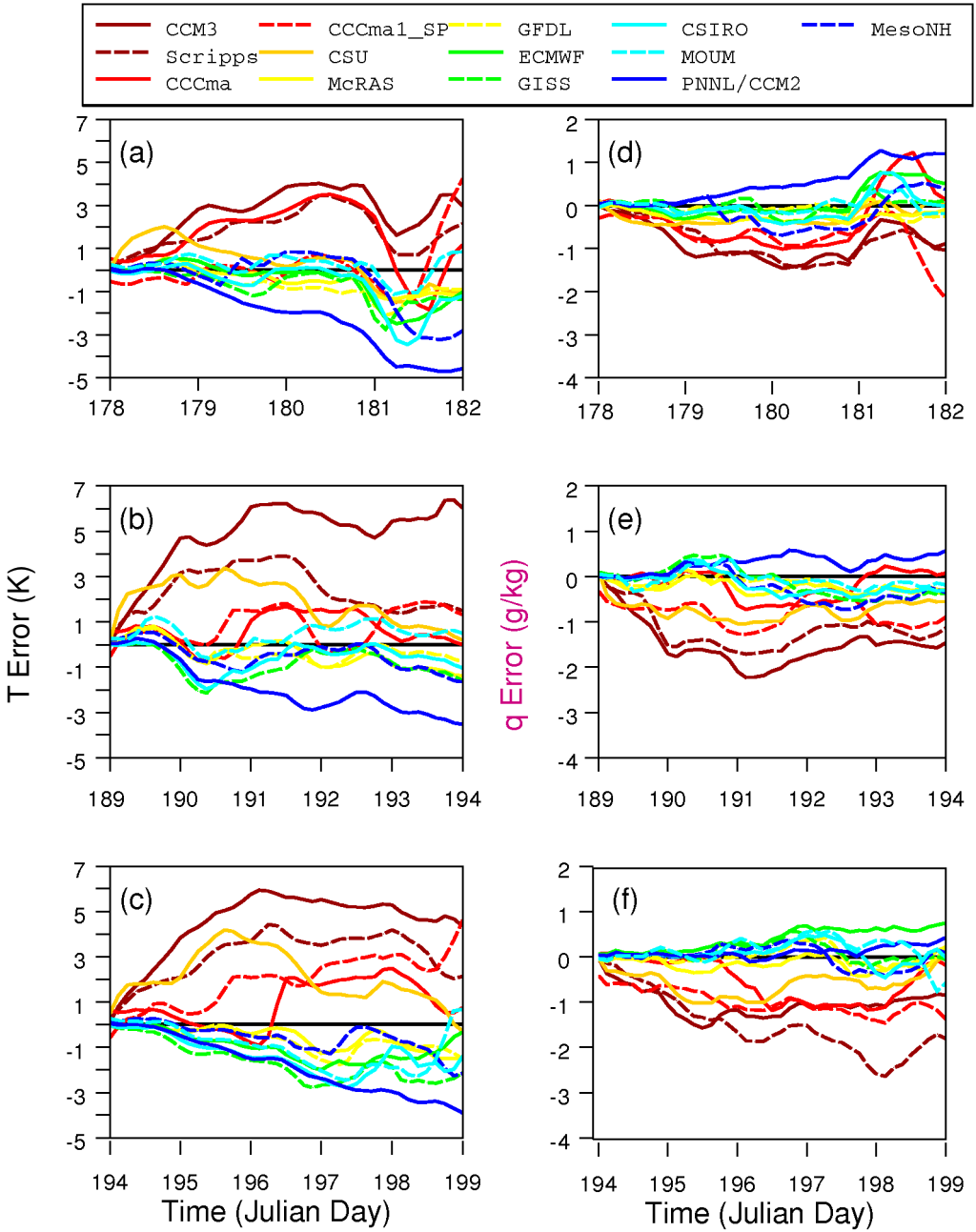
Figure 9. Time evolution of the column mean (between pressure levels 115 to 915 hPa): (a), (b) and (c) temperature errors produced by the single-column models for Subcases A, B and C, respectively; (d), (e) and (f) similar but for moisture. Models shown in the key are discussed in the text.
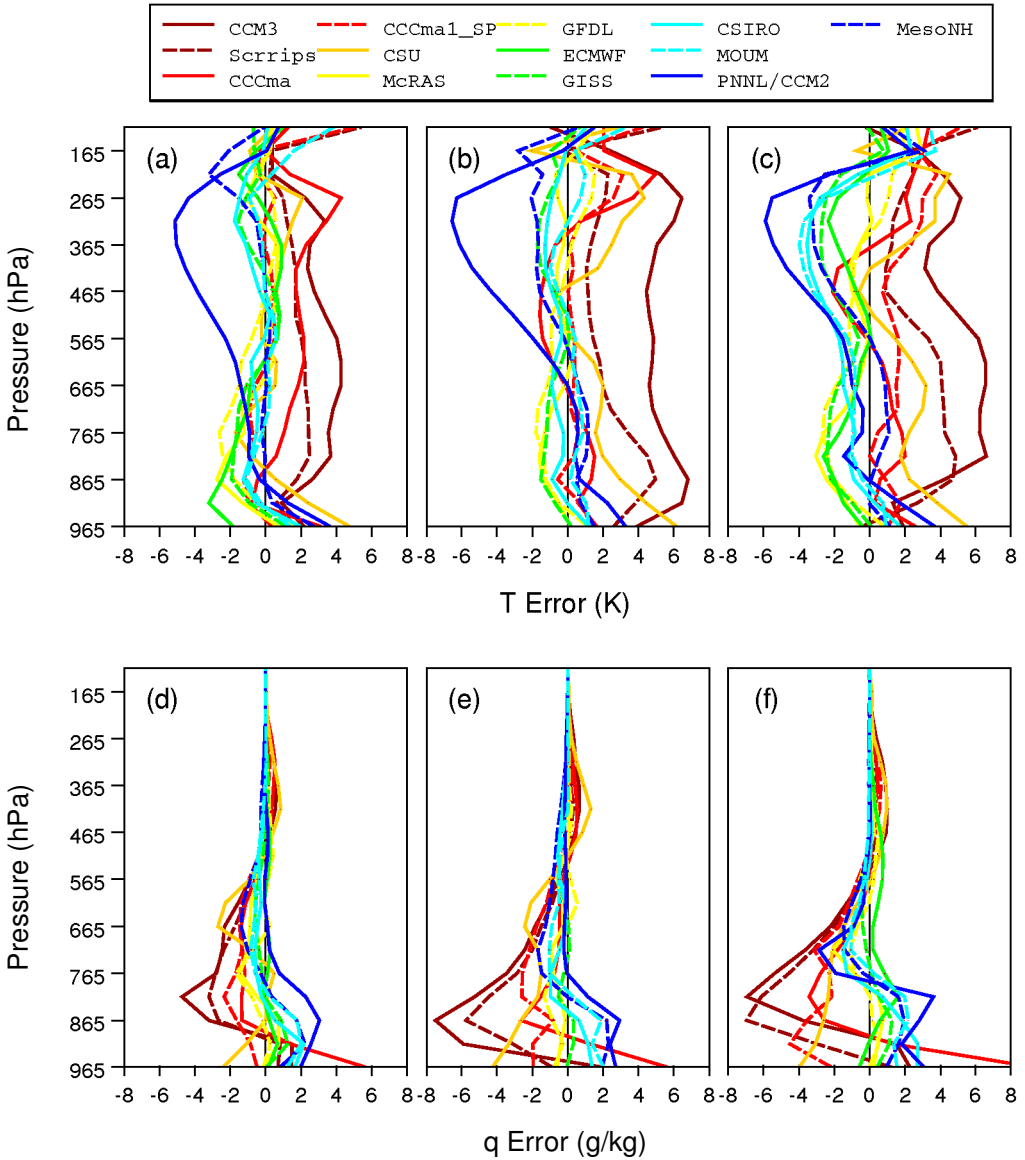
Figure 10. Vertical profiles of time-averaged: (a), (b) and (c) temperature errors produced by the single-column models over Subcases A, B and C, respectively; (d), (e) and (f) similar but for moisture errors. Models shown in the key are discussed in the text.

(see Table 2). CCM3 and PNNL/CCM2 are the two typical cases: the former shows the largest warm biases and the latter shows the largest cold biases in the middle and upper troposphere. It is also noteworthy that a majority of models produce warm biases near the surface, suggesting possible errors in the specified surface fluxes and surface temperature. Besides, deficiencies in PBL parametrizations and weak downdraughts in SCMs (see section S4(d)) may also account for the large errors near the surface.

For moisture (Figs. 10(d)–(f)), McRAS, GFDL, GISS and ECMWF have rather small biases in the entire troposphere, comparable to CRMs (Xu *et al.* 2002). However,

at least five SCMs show much drier atmospheres than given by the observations between 500–800 hPa. This may be partly related to weak downdraught mass fluxes produced in SCMs, since evaporation of precipitation within cloud and mesoscale downdraughts acts to cool and moisten the convecting atmosphere. The moisture biases have large inter-model differences in the entire troposphere, especially below 765 hPa. Dry biases are associated with warm biases, and moist biases with cold biases in the lower troposphere. It is also noted that CCCma has extremely large moist biases near the surface. This is related to the large moistening produced from its turbulence parametrization (Lohmann 2001, personal communication).

Compared to SCMs, CRMs show much smaller biases in the simulated temperature and moisture and much smaller inter-model differences (Fig. 5 in Xu *et al.* 2002). The temperature biases are typically less than 1.5 K below 12 km and the moisture biases are within 0.5 g kg^{-1} for most CRMs. Considering that the cloud-scale processes are explicitly resolved in CRMs, the CRM results further suggest that deficiencies in SCM cloud parametrizations are responsible for considerable amounts of the biases in thermodynamic fields. Furthermore, the magnitudes of the CRM biases also provide a target for SCMs to further improve their parametrizations.

(d)   Cloud mass flux

Cloud mass fluxes are highly related to convective heating/drying profiles; however, they are usually not easy to observe. In this study we make use of the cloud mass fluxes diagnosed from CRMs to evaluate those produced from SCMs. The criteria for diagnosing updraught (M_u), downdraught (M_d) and net mass fluxes (M_c) from CRMs data are given in Xu *et al.* (2002).

Figures 11(a)–(c) compare the vertical structure of M_u, M_d and M_c, respectively, estimated from the SCMs with those diagnosed from the CRMs averaged over precipitation periods (i.e. with observed precipitation rate $\geqslant 0.36$ mm day^{-1}) of Subcases A, B and C. Figures 11(d)–(f) are identical to Figs. 11(a)–(c) but for non-precipitation periods (observed precipitation rate < 0.36 mm day^{-1}). It should also be noted that the radiative heating rate is specified from the ECMWF analysis in the CRM simulations. The solid black lines in Figs. 11(c) and (f) are the observed large-scale mean mass flux ($M = -\omega$). A detailed description of individual CRM results can be found in Xu *et al.* (2002). Data for the updraught and downdraught mass fluxes are not available for ECMWF and GFDL, and three SCMs (i.e. CSU, GFDL, and PNNL/CCM2) do not have downdraught parametrizations.

During precipitation periods (Figs. 11(a)–(c)), the CRMs show large M_u in the middle and upper troposphere between 300 and 700 hPa; M_d has a magnitude comparable with M_u, the maximum M_d is around 600 hPa. As a result, M_c is relatively small compared to M_d and M_u; it is positive in the middle and upper troposphere and negative in the lower troposphere. As shown in Raymond (1993), this is a typical vertical structure of the net cloud mass fluxes in cumulonimbus clouds in midlatitudes where cloud base heights and PBL depths are usually higher and the precipitation induced downdraughts can equal or exceed updraughts in the lower parts of cumulonimbus clouds.

Compared to the CRMs, the updraught mass flux in the SCMs is smaller in the middle and upper troposphere and larger in the lower troposphere. The latter is associated with lower cloud base heights in SCMs. The downdraughts in the SCMs are very weak. This leads to much larger net mass fluxes in virtually all SCMs, especially in the lower troposphere. Most models fail to produce the negative mass flux shown in the CRMs due
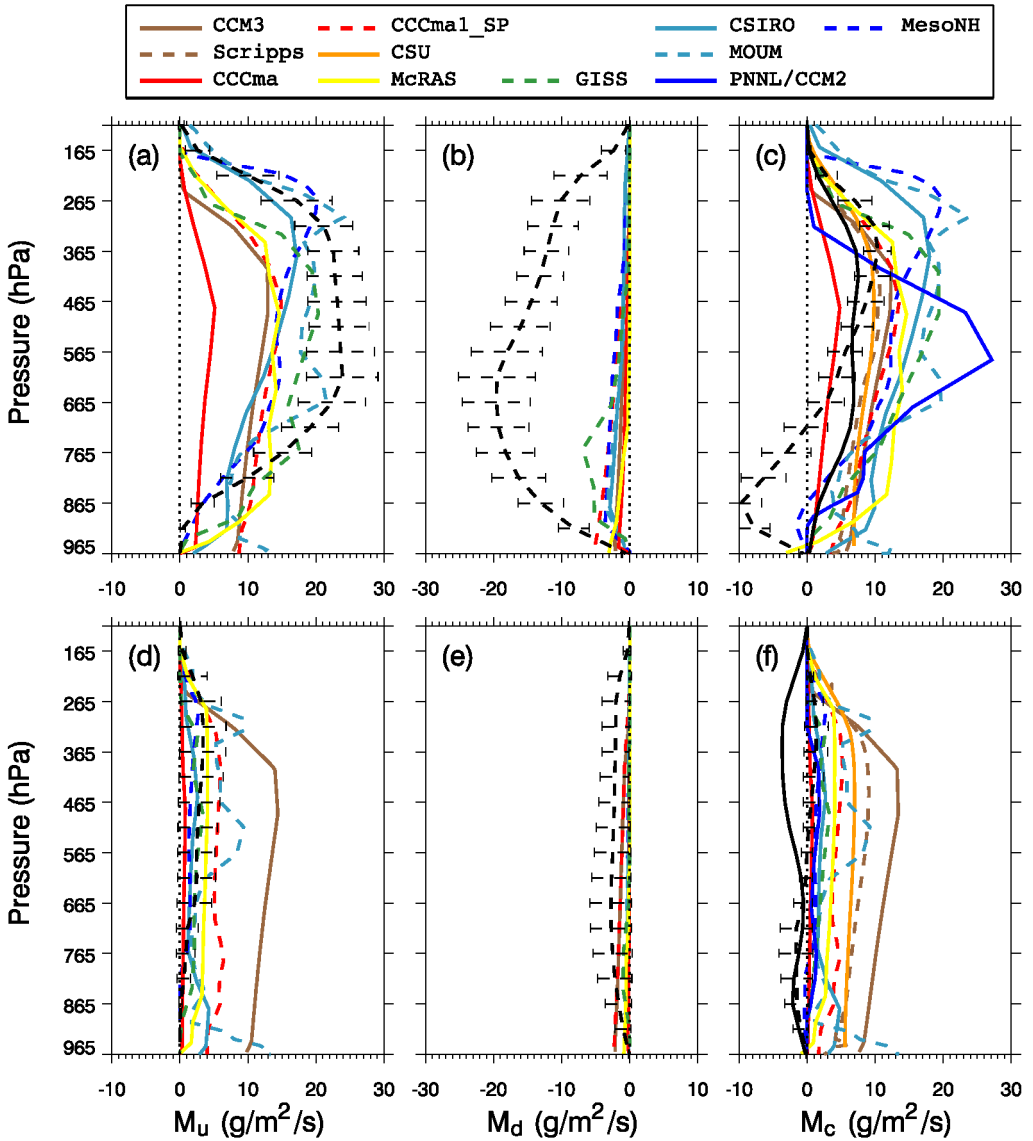
Figure 11. Vertical profiles of updraught, downdraught and net cloud mass fluxes averaged over precipitation periods (observed precipitation rates $\geqslant 0.36$ mm day^{-1}) and non-precipitation periods (observed precipitation rates < 0.36 mm day^{-1}) of Subcases A, B and C. Black solid lines are observed large-scale mean mass fluxes ($-\omega$); black dashed lines and small bars represent the means and standard deviations of the mass fluxes across the ten cloud-resolving models which are given in the key and discussed in the text: (a), (b) and (c) represent the updraughts, downdraughts and net cloud mass fluxes, respectively, during precipitation periods; (d), (e) and (f) are similar but for non-precipitation periods.

to the weak downdraughts and lower cloud base heights. Only MesoNH exhibits small negative mass flux in the lower troposphere because of its higher cloud base heights.

It should be noted that there are differences in defining cloud mass fluxes between CRMs and SCMs. In the CRMs, the cloud mass fluxes contain all types of updraughts and downdraughts including those of convective-scale and mesoscale. In contrast, the
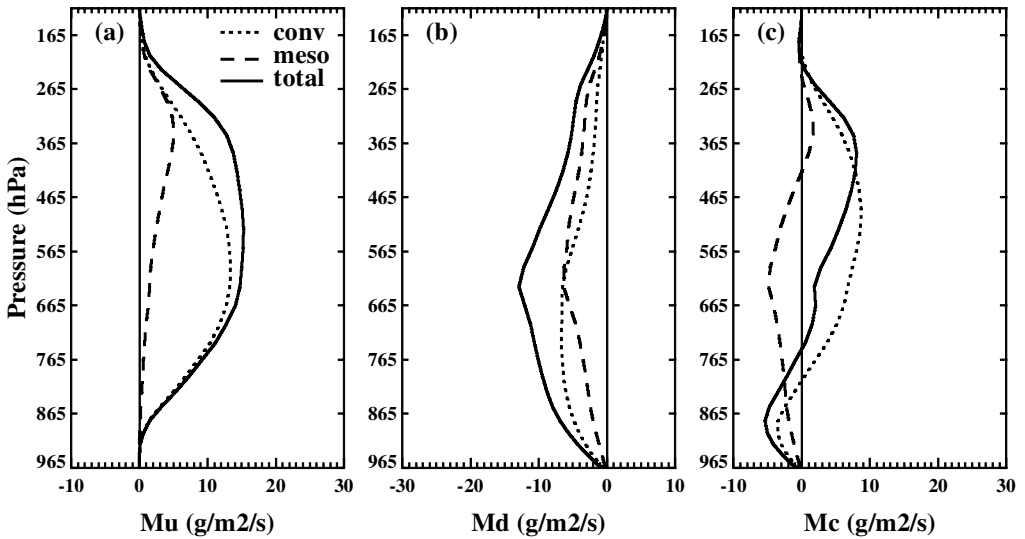
Figure 12. Vertical profiles of: (a) updraught, (b) downdraught, and (c) net cumulus mass fluxes estimated from the UCLA/CSU cloud-resolving model averaged over the precipitation periods of Subcases A, B and C. Solid lines represent the total mass fluxes, dotted lines convective-scale contributions and dashed lines mesoscale contributions.

SCMs only parametrize convective-scale updraughts and convective-scale precipitation-induced downdraughts (see Table 3). This can partly explain why the differences are so large. Many studies (e.g. Johnson 1980; Houze and Cheng 1981; Cheng and Yanai 1989) have shown that mass fluxes in mesoscale updraughts and downdraughts are significant relative to convective mass fluxes.

The mesoscale and convective-scale mass fluxes diagnosed from the UCLA/CSU CRM are used to discuss the importance of mesoscale updraughts and downdraughts (Fig. 12). These data are not available from other CRMs. The mass fluxes are averaged over the same precipitation periods as those in Figs. 11(a)–(c). The partitioning method used for this analysis is described in Xu (1995). The maximum draught velocity below the melting level is the main variable used to distinguish convective regions from stratiform regions. An entire CRM column is classified as a convective region if the maximum draught velocity is at least twice the averaged value of two adjacent grid columns, or exceeds 3 m s^{-1}, or the surface precipitation rate exceeds 25 mm h^{-1}. Some other variables are also used to diagnose shallow convection columns. In addition, some gravity-wave contributions are eliminated from the mass flux profiles by raising the thresholds on the condensate mixing ratios to $3 \times 10^{-4} \text{ g g}^{-1}$ when draught velocities are less than 1 m s^{-1}. Table 6 provides time-means (all three subcases combined) of total, convective and stratiform precipitation rates, as well as the ratio of the convective and stratiform precipitation to the total precipitation, for the CRM and ABRFC radar estimates. It is seen that the CRM-produced surface precipitation rates are in an excellent agreement with the observations. The stratiform and convective components from the CRM are also very close to the observational estimates. This provides confidence in the partition of the convective-scale and mesoscale mass fluxes from this CRM.

The UCLA/CSU CRM results indicate that convective-scale updraughts are a major contributor to the total updraught mass flux at levels below 300 hPa (Fig. 12(a)). Its maximum mass flux appears in the middle troposphere ($\sim$600 hPa) while the counterpart

TABLE 6. SURFACE PRECIPITATION RATES
(mm DAY^{-1}) AVERAGED OVER SUBCASES A, B AND C

	UCLA/CSU CRM	Observations
Total	5.56	5.51
Convective	4.04	3.98
Stratiform	1.52	1.53
Convective/total	0.73	0.72
Stratiform/total	0.27	0.28

of mesoscale updraughts appears in the upper troposphere ($\sim$300 hPa). In contrast to the updraughts, mesoscale downdraughts have values comparable with convective-scale downdraughts (Fig. 12(b)). The convective-scale downdraughts are mainly located in the lower troposphere. For the net mass fluxes, the convective-scale mass flux is dominated by the convective-scale updraughts throughout the entire troposphere except for the levels below 800 hPa, while the mesoscale mass flux is dominated by the mesoscale downdraughts in the lower and middle troposphere (Fig. 12(c)). It is seen from Figs. 11(a) and (b) that the SCMs generally capture well the convective-scale updraughts, but most of the SCMs still significantly underestimate the convective-scale downdraughts except for GISS. Most SCMs have higher maximum convective-scale updraught levels (400 hPa) than the CRM (600 hPa). Nevertheless, a firm conclusion cannot be drawn from this comparison, due to noticeable differences among the CRMs (Fig. 11).

It should be noted that large uncertainties remain in the mass flux diagnosed from the CRMs and the methodology used for partitioning the total mass flux into convective-scale and mesoscale components. The presence of these uncertainties does not allow one to fully explain the large discrepancies between the SCMs and the CRMs. For example, Xu *et al.* (2002) show that the diagnosed mass fluxes in the CRMs include contributions not only from convective-scale and mesoscale circulations but also from gravity waves, since many different scales of motions are present in CRM simulations. Therefore, some updraught and downdraught mass fluxes in the upper troposphere may be related to unrealistically strong gravity-wave activities in the simulations.

The weak downdraughts in SCMs are also related to the assumptions made in the parametrizations. For example, downdraughts in SCMs are limited so as not to exceed certain amounts of the corresponding updraughts. Some schemes (e.g. ZM) assume that no downdraughts are allowed below cloud base (see Table 3). In addition, too strong downdraughts may overly suppress subsequent convection. An independent study (Bechtold 2001, personal communication) shows that downdraughts can be tuned to give the right strength and good lower level temperature and moisture biases corresponding to the CRM results, but the precipitation obtained was too low.

During non-precipitation periods (Figs. 11(d)–(f)), the updraught, downdraught and net cloud mass fluxes diagnosed from all CRMs are close to zero. However, some SCMs such as CCM3, Scripps, CSU and CCCma1_SP generate large cloud mass flux during non-precipitation periods. This is closely related to the problem with triggering convection, as discussed earlier.

Figure 11 also shows considerable inter-model differences among the SCMs. In general, the CCM3, Scripps, CCCma1_SP and CSU produce smaller (larger) mass fluxes than the others during precipitation (non-precipitation) periods. This suggests that the warm and dry biases found in these models are mostly related to the spurious convections generated over the non-precipitation periods. On the other hand, M_c in PNNL/CCM2 (Fig. 11(c)) is significantly smaller in the upper troposphere than other SCMs. The M_c is mainly located in the middle and lower troposphere with the maximum

value around 600 hPa. Compared to other SCMs, PNNL/CCM2 typically has a higher cloud base and a lower cloud top, which imply that this model, with a non-penetrative convection scheme, underestimates the depth of instability. It is also noted that CCCma produces the weakest cloud mass flux. This is consistent with the fact that this model overly suppresses convection as shown earlier.

(*e*)   *Apparent heat sources, Q1, and moisture sinks, Q2*

The time-averaged apparent heat sources ($Q1$, Yanai *et al.* 1973) and contributions from individual physical processes such as radiative heating (Qr), cumulus convection ($Q1c$) and turbulent processes ($Q1v$), over precipitation and non-precipitation periods of Subcases A, B and C are examined next. Note that the contributions from individual physical processes are not available from some models. During precipitation periods, the observed $Q1$ shows strong heating in the upper troposphere and weak cooling below 765 hPa (Fig. 13(a)); the maximum heating is at about 400 hPa. Most models reproduce well the observed $Q1$ above 700 hPa, while CCM3, Scripps and CCCma1_SP overestimate the heating in the lower levels. Consistent with the weak mass fluxes, PNNL/CCM2 greatly underestimates the strong heating in the upper troposphere. This contributes to its large cold biases seen in the upper troposphere.

It is also seen that convective heating ($Q1c$) contributes the most to the total $Q1$ for the levels above 865 hPa for all models. Below 865 hPa, radiative cooling (Qr) and turbulent processes ($Q1v$) also have significant contributions to the total $Q1$ (Figs. 13(b)–(d)). Consistent with the small stratiform precipitation produced in the models, contributions from stratiform clouds are very small (not shown).

During non-precipitation periods, the observations show very weak heating and cooling (Fig. 14(a)). Compared to the observations, the models with the CAPE-only triggers and CSU produce excessive warming in the middle and upper troposphere. This excessive warming is a major contributor to the warm biases seen in Figs. 10(a)–(c). The individual components clearly show that model cumulus convection ($Q1c$) is the major reason for the excessive warming. In fact, the inter-model differences are small in other components compared to those in $Q1c$ except for the boundary layer where $Q1v$ also shows rather large inter-model differences (Figs. 14(b)–(d)).

The apparent moisture sinks ($Q2$) were introduced by Yanai *et al*. (1973), representing moisture changes due to condensation, evaporation and subgrid-scale transport. The time-averaged $Q2$ and the contributions from individual physical processes such as cumulus convection ($Q2c$) and turbulent processes ($Q2v$), over precipitation and non-precipitation periods of the three subcases, are shown in Figs. 15 and 16, respectively. During precipitation periods, the calculated $Q2$ from the models agrees closely with the observed $Q2$ above 765 hPa while the models diverge below (Fig. 15(a)). In general, the models with the CAPE-only triggers show excessive drying and the others show excessive moistening. It is seen that convective drying is a major contributor to the total drying above 750 hPa (Fig. 15(b)). Below that level, drying from $Q2c$ and moistening from $Q2v$ have comparable contributions to the total $Q2$ but of opposite sign (Fig. 15(c)). During non-precipitation periods (Fig. 16) these models show considerable inter-model differences in $Q2$. The models with CAPE-only triggers generally produce strong drying in the middle and lower troposphere, which is mainly related to the excessive convective drying ($Q2c$) generated in these models during non-precipitation periods. This is consistent with the results seen in the simulated moisture field (Figs. 10(d)–(f)).
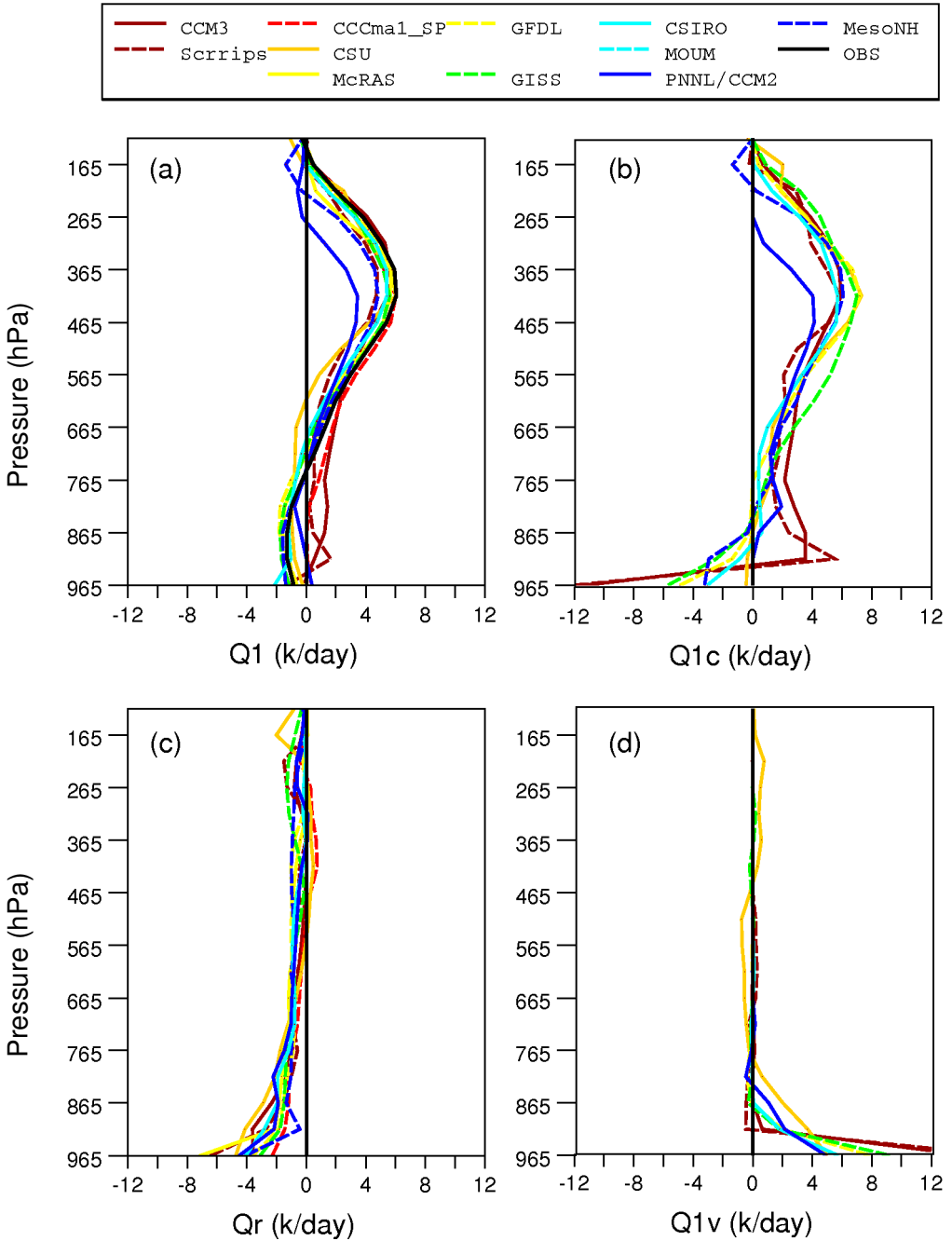
Figure 13. (a) Apparent heat sources ($Q1$) averaged over the precipitation periods (observed precipitation rates $\geqslant 0.36$ mm day^{-1}) of Subcases A, B and C (K day^{-1}); (b), (c) and (d) contributions from cumulus convection ($Q1c$), radiation (Qr) and turbulent processes ($Q1v$), respectively. Models shown in the key are discussed in the text.
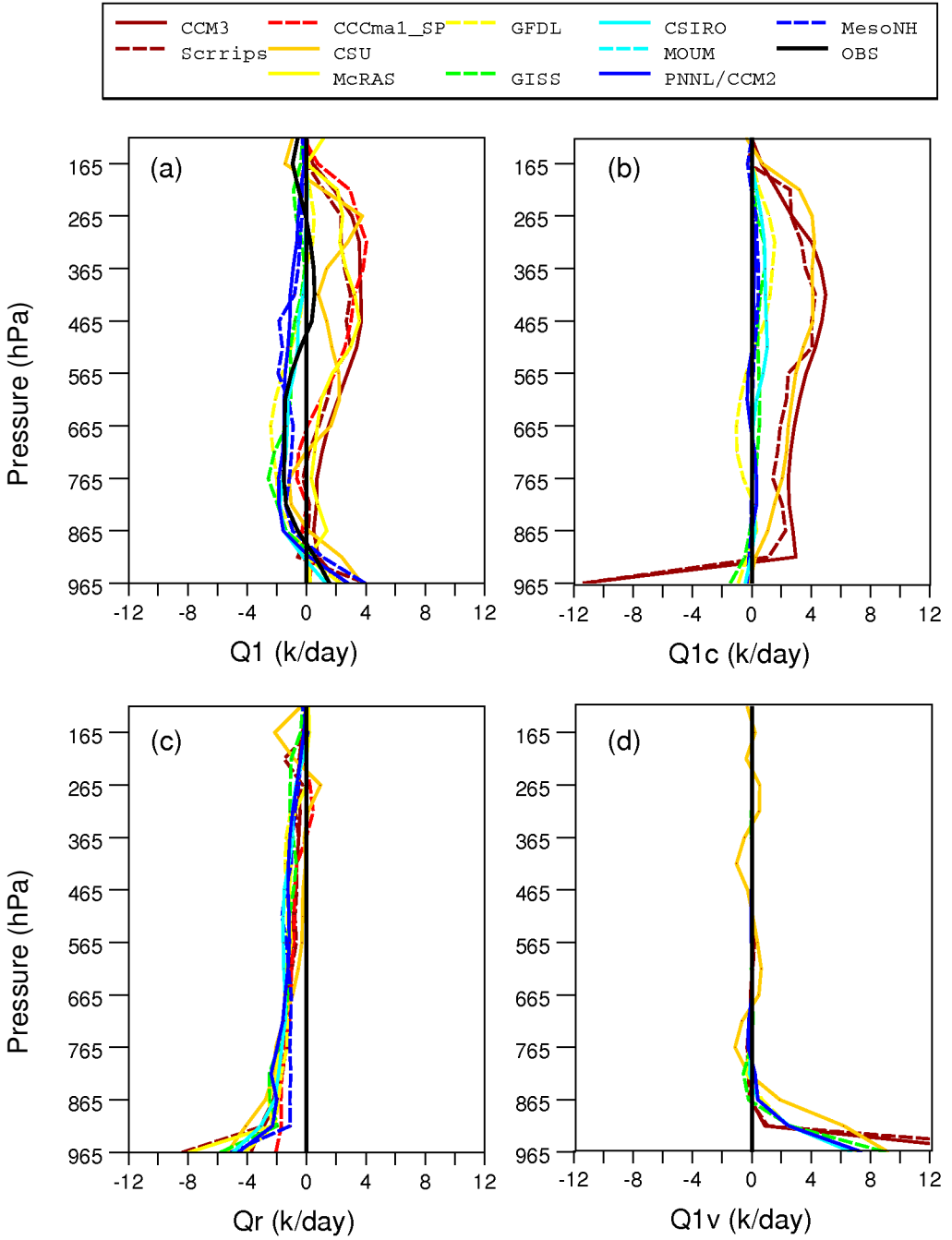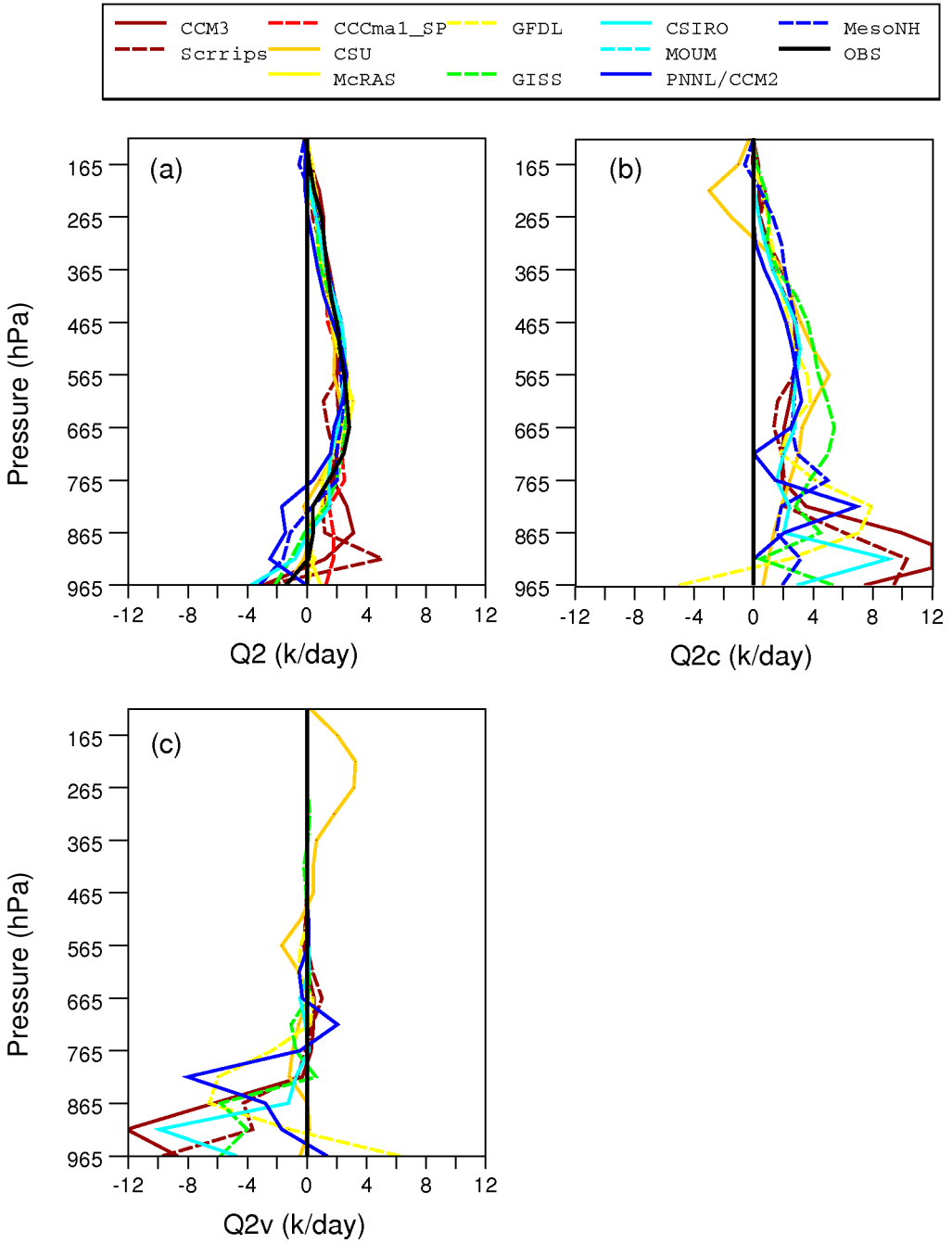
Figure 14. Same as Fig. 13 but for non-precipitation periods (observed precipitation rates < 0.36 mm day^{-1}) of Subcases A, B and C.

Figure 15. (a) Apparent moisture sinks ($Q2$) averaged over precipitation periods (observed precipitation rates $\geqslant$ 0.36 mm day^{-1}) of Subcases A, B and C (K day^{-1}); (b) and (c) similar but contributions from cumulus convection ($Q2c$) and turbulent processes ($Q2v$), respectively. Models shown in the key are discussed in the text.
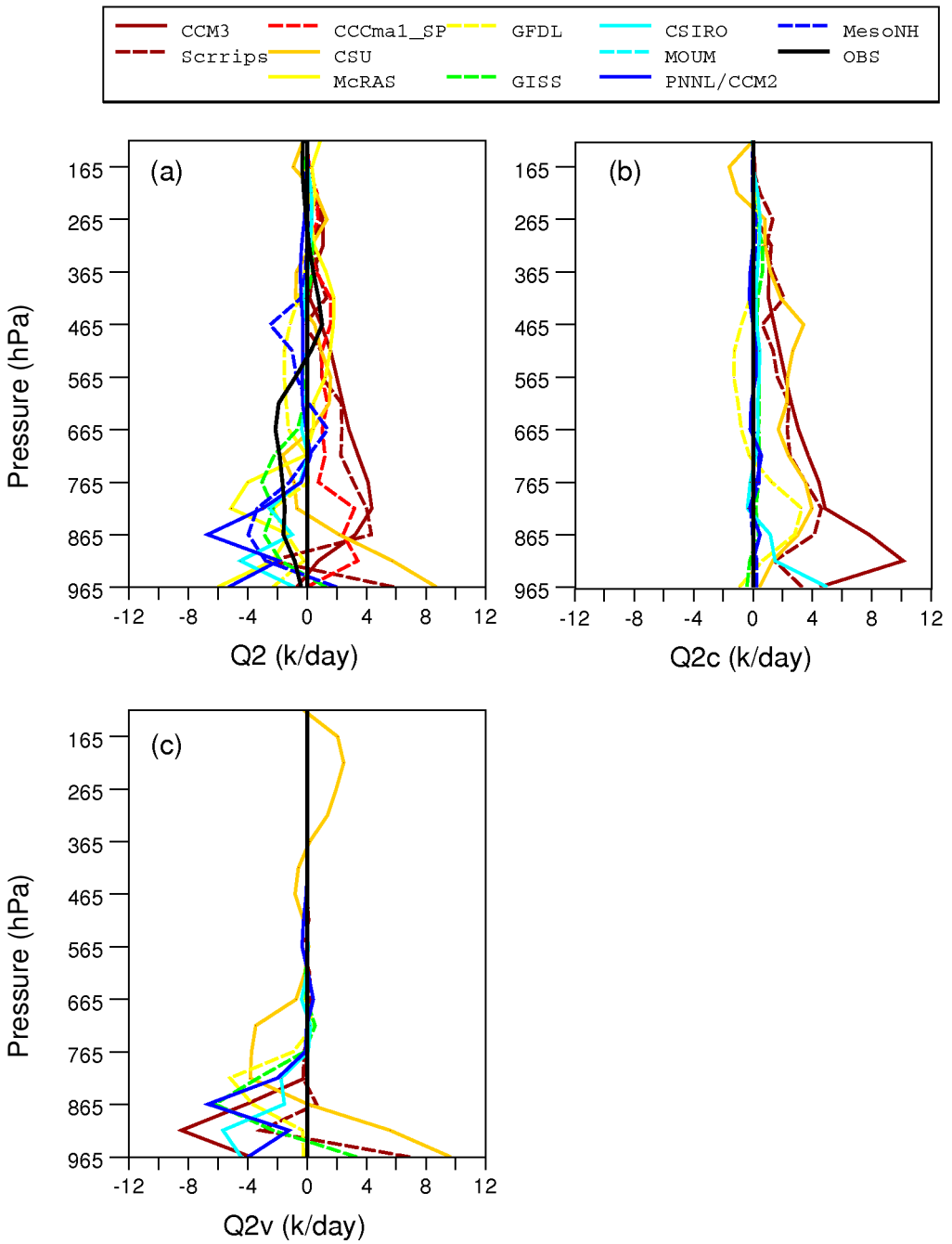
Figure 16. Same as Fig. 15 but for the non-precipitation periods (observed precipitation rates < 0.36 mm day^{-1}) of Subcases A, B and C.

5. Sensitivity tests

In the previous section, we have discussed the simulation results of thirteen SCMs from the baseline experiment. In this section we investigate the sensitivity of these results to different forcing approaches. We also show results from CCM3 with some improvements to its deep convection scheme (ZM). It should be noted that not all SCMs participated in the sensitivity tests.

(a) Nudging approach

The nudging approach specifies the total advective tendency from the observations, and the simulated temperature and moisture are nudged toward the observations at each time step. A detailed description of this approach can be found in Ghan *et al.* (2000). Using the nudging approach can help reduce impacts from errors produced in the previous time step on simulations in the next time step.

With the nudging approach, the models that have problems in their triggering mechanisms, such as CCM3, Scripps and CSU, still significantly overestimate the precipitation rates during non-precipitation periods (Figs. 17(a) to (c)). The surface rainfall produced from these models shows clear diurnal variations. This problem is not as significant in the rest of the models. This is consistent with the results seen in the baseline experiment.

(b) Forcing with a specified radiative heating rate

This forcing method is identical to the baseline experiment except that the radiative heating rate (Qr) is specified from the ECMWF analysis. This removes one more uncertainty in the multi-model intercomparison study. Here we only show the simulation results of precipitation, temperature and moisture for Subcase B (Figs. 18(a)–(c)). Temperature and moisture errors (Figs. 18(b) and (c)) are averaged between 115 and 915 hPa. A main conclusion from this sensitivity test is that most of the models show results similar to the baseline experiment. However, CCCma and PNNL/CCM2 show some sensitivity to this forcing approach. CCCma misses the first two precipitation events, while it overestimates the last convective event when Qr is fixed. In the baseline experiment this model greatly underestimates almost all the precipitation events. It also shows cold/moist biases in Figs. 18(b) and (c) in contrast to the warm/dry biases in Figs. 9(b) and (e). By using the specified radiative heating rate, PNNL/CCM2 generally shows a warm bias instead of the cold bias in the baseline experiment, due perhaps to inadequate cloud–radiation interactions.

(c) Sensitivity tests to triggering mechanism and closure assumption

As mentioned before, among the models participating in the intercomparison, CCM3, CCM3/SIO and CCM3/SUNY are identical in every aspect except for the parametrization of convection. Thus the differences among these models would give a measure of the sensitivity of the simulations to convective parametrization. CCM3/SUNY uses a triggering mechanism proposed by Xie and Zhang (2000). They link the convective triggering mechanism with the large-scale dynamic forcing based on the observations to overcome the problem of using the CAPE-only trigger in ZM. They assume that model convection occurs only when the large-scale dynamic forcing makes positive contributions to the existing positive CAPE. Zhang (2002) took a further step and used the large-scale tropospheric forcing (without the boundary-layer forcing) to determine not only the timing but also the amount of convection. He modified the CAPE
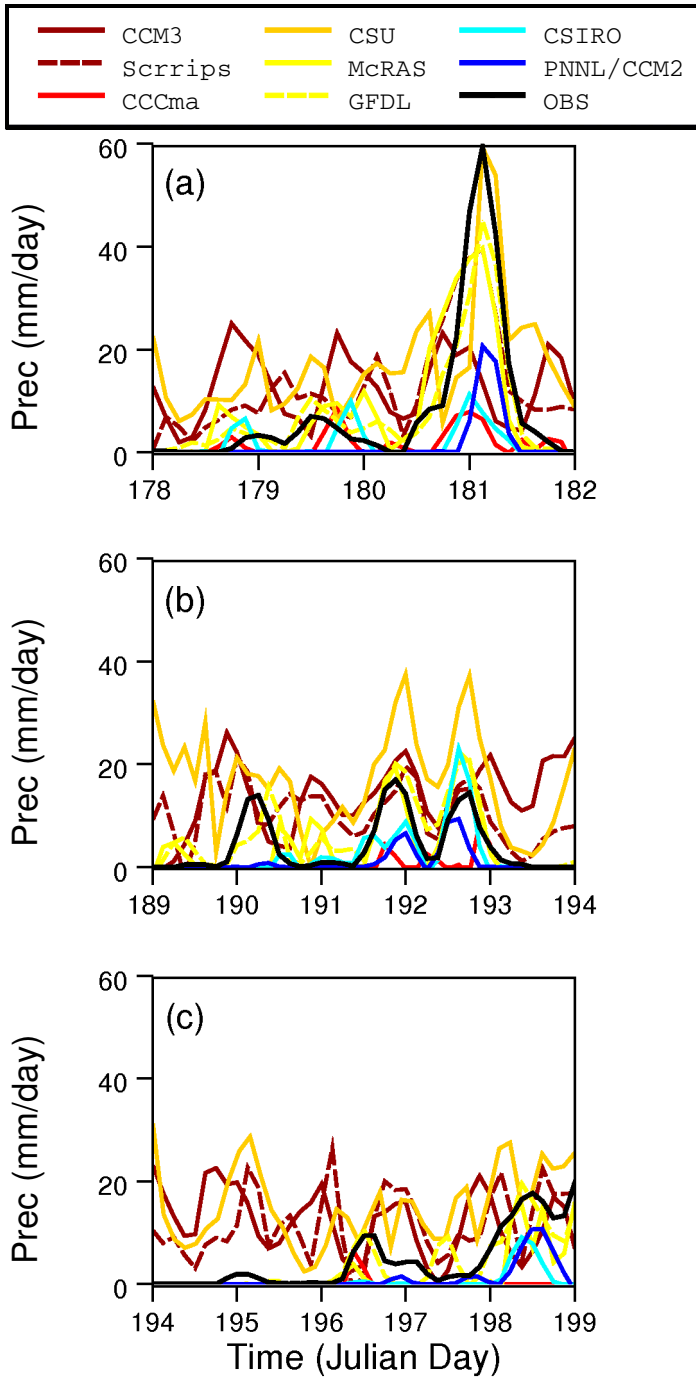
Figure 17. Time series of the observed and simulated surface total precipitation rates using the nudging approach: (a), (b) and (c) for Subcases A, B and C, respectively. Models shown in the key are discussed in the text.
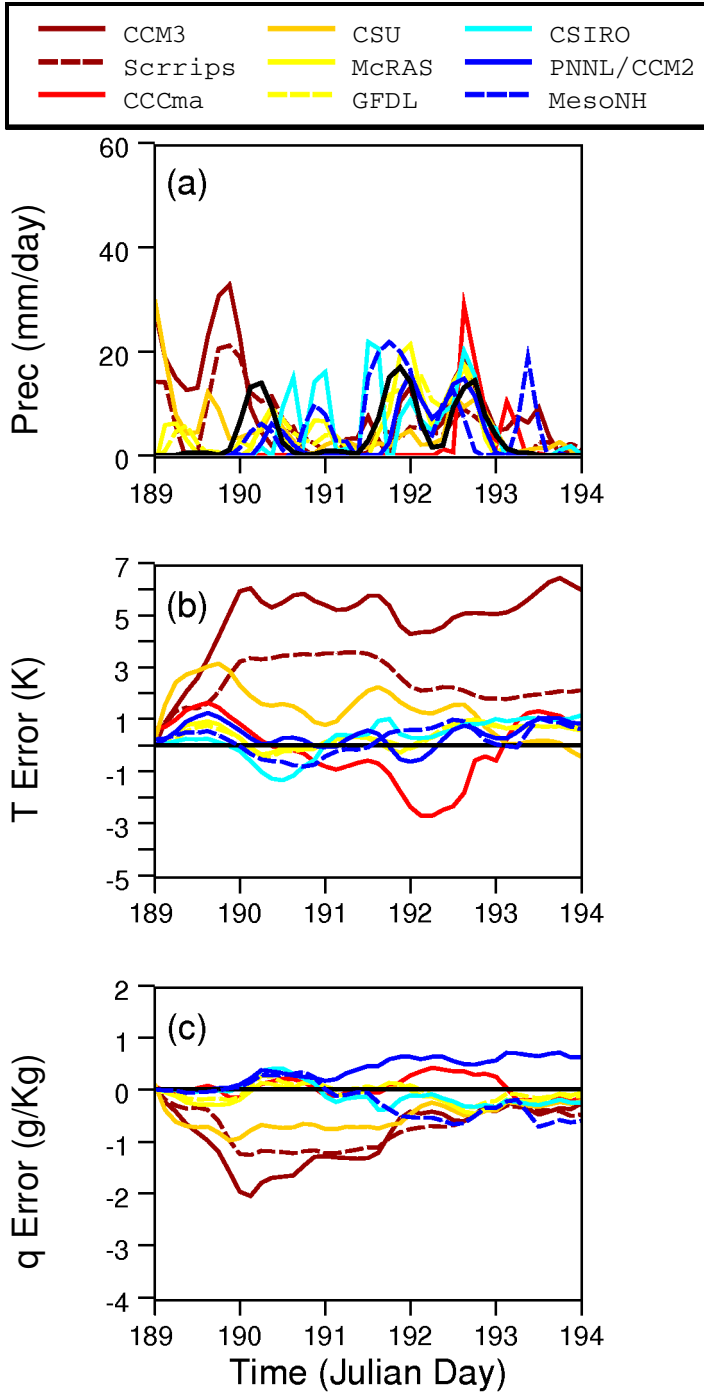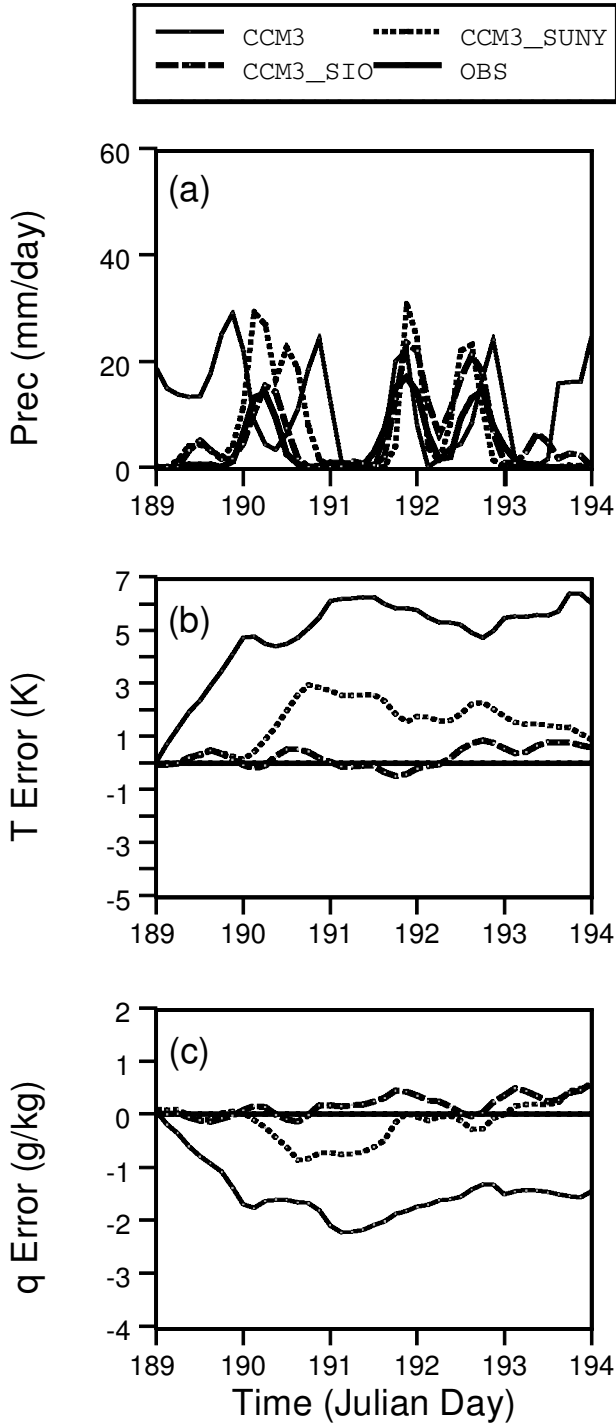
Figure 18. Time series of: (a) the observed (black line) and simulated surface total precipitation rates produced by the single-column models for Subcase B, using the forcing with a specified radiative heating rate; (b) and (c) as (a), but the column-mean temperature and moisture errors, respectively, between pressure levels 115 and 915 hPa. Models shown in the key are discussed in the text.

Figure 19. Time series of: (a) the observed (thick solid line) and simulated total surface precipitation rates produced by the single-column models for Subcase B, using the same forcing approach as in the baseline experiment; (b) and (c) as (a) but the column-mean temperature and moisture errors, respectively, between pressure levels 115 and 915 hPa. Models shown in the key are discussed in the text.
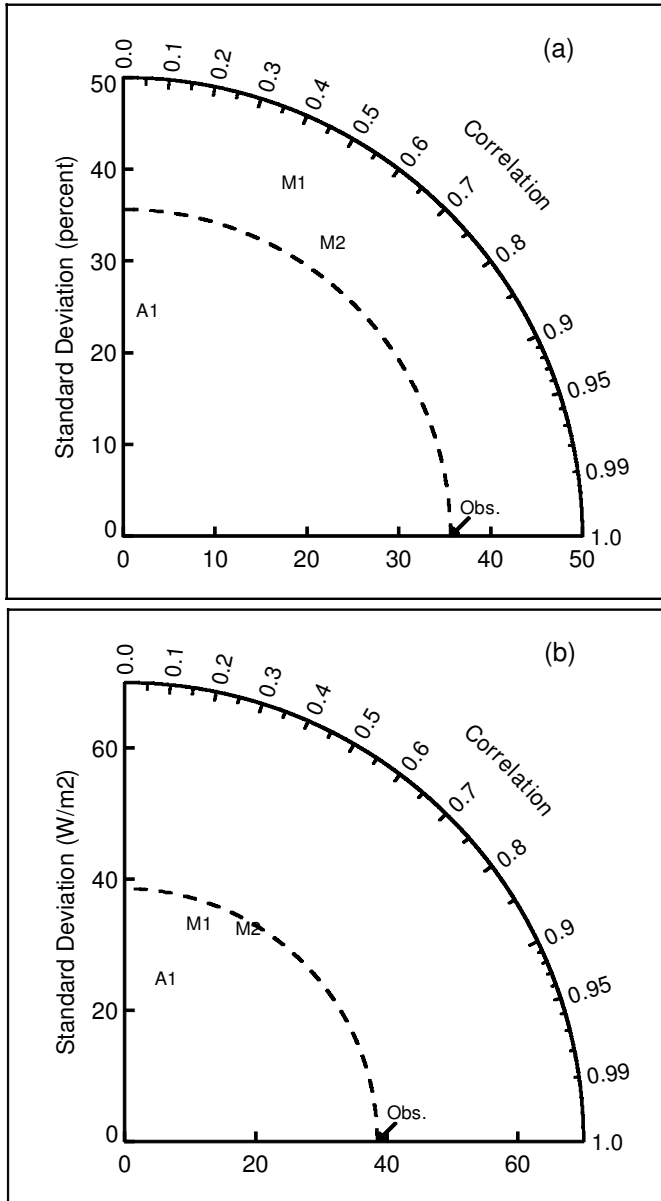
Figure 20. A Taylor diagram comparing: (a) column cloud fraction and (b) outgoing long-wave radiation at the top of the atmosphere, produced from models CCM3, CCM3/SUNY and CCM3/SIO. Point A1 denotes CCM3, point M1 CCM3/SUNY and point M2 CCM3/SIO. See Fig. 5 for an explanation of the diagram, and the text for a discussion of the models.

closure for ZM so that the cloud base mass flux is determined by the CAPE generation rate due to the tropospheric forcing. The new closure assumption is used in CCM3/SIO.

Figures 19(a)–(c) show time series of the simulated precipitation rates, the averaged temperature biases and the average moisture biases, respectively, between 115 and 915 hPa from CCM3, CCM3/SUNY and CCM3/SIO for Subcase B, using the forcing approach in the baseline simulation. It is seen that both the revised ZM schemes

generally reproduce the observed precipitation rates well, even for the first convective event of Subcase B which almost all SCMs and CRMs fail to capture. This is because the overall large-scale forcing is strong enough to destabilize the atmosphere and make convection happen even though there is large-scale moisture divergence in the lower troposphere observed in this event (Fig. 3(e)). As a result, the large warm/dry biases shown in CCM3 are greatly reduced in CCM3/SUNY and CCM3/SIO. Compared to CCM3/SIO, CCM3/SUNY captures the timing well but overestimates the magnitude of convection; thus, larger errors are produced in the temperature and moisture fields. In CCM3/SUNY the same closure assumption is used as in the original ZM scheme, while it is revised in CCM3/SIO; this significantly reduces the biases in CCM3/SIO.

Cloud and radiation fields are also improved with the improved triggering mechanism and closure assumption. Figures 20(a) and (b) show the Taylor diagram for column cloud fraction and OLR at the TOA, respectively, for Subcase B. In Fig. 20, A1 denotes CCM3, M1 denotes CCM3/SUNY, and M2 denotes CCM3/SIO. Both the revised ZM schemes (points M1 and M2) improve the simulation of clouds and OLR in terms of the correlation coefficient, the temporal variability and the RMS errors in comparison with the original ZM scheme (point A1).

6.   CONCLUSION

Using the observations from the Summer ARM 1997 IOP and the data diagnosed from ten CRMs, 15 SCMs have been evaluated under summertime midlatitude continental conditions with a focus on their cumulus parametrizations. The baseline experiment shows that most SCMs can reasonably reproduce the observed precipitation events that were well-developed within the SCM domain. For those convective systems that are partly located within the SCM domain and occupied a small part of the domain, it has been shown that the domain-averaged large-scale forcing may not properly capture their characteristics; one result from this is the failure of most models to simulate these precipitation events. It should be noted that one could not expect SCMs to be able to correctly predict every single convective event, given the current SCM domain size of 370×300 km^2. However, knowledge of pdfs of thermodynamic properties in the boundary layer may help SCMs to get the statistics of convection occurrence right.

It has been shown that deficiencies associated with convective triggering mechanisms are mainly responsible for the large errors produced in some models. Convection in those models that use triggers based on the vertical integral of parcel buoyant energy is more active than in those that use local parcel buoyancy if no additional constraint is used to control the onset of continental convection. The overactive convection leads to large systematic warm/dry biases in the troposphere in these models. It is also shown that a model with a non-penetrative convection scheme produces large systematic cold/moist biases in the troposphere due to underestimation of the depth of instability.

The radar-estimated surface precipitation data show that stratiform precipitation has a considerable contribution (28%) to the total precipitation during the three precipitation periods chosen for this study. This is, however, not reproduced by SCMs; that is, the simulated surface precipitation is mainly from cumulus clouds for virtually all SCMs.

The updraught mass fluxes in the SCMs agree well with those in the CRMs. In contrast, most SCMs produce very weak downdraught mass fluxes compared with those diagnosed from the CRMs. This leads to larger net mass fluxes in the SCMs, especially in the lower and middle troposphere. As a result, most SCMs fail to produce the negative net mass fluxes in the lower troposphere shown in the CRMs. Neglect of mesoscale circulations in the SCMs, uncertainties in the diagnosed mass fluxes

from the CRMs and problems with cumulus parametrizations, such as the cloud base height and assumptions for downdraughts, are all responsible for the discrepancies. In future, parametrization of mesoscale circulations needs to be incorporated into the models (e.g. Donner 1993; Xu 1995), in addition to further improvement of convective downdraught formulations in most SCMs. Reducing the uncertainties in the CRM mass fluxes, such as eliminating gravity-wave contributions to the updraughts and downdraughts, is also needed so that CRMs can provide more reliable information for SCMs to improve their physical parametrizations.

It should be noted that deficiencies from other model parametrizations, such as radiation, cloud and turbulence schemes, could also affect the SCM simulations. From the heat and moisture budget analysis, however, this study has shown that convective heating and drying contribute most to the large inter-model differences in the troposphere. The inter-model differences from other physical processes are relatively small, compared to those from cumulus convection, except in the boundary layer. This may be related to the cases selected in this study which are mainly dominated by strong cumulus convection. It may also suggest that the interaction between convective and stratiform precipitation processes is not properly formulated in SCMs. Nevertheless, a detailed analysis of the interactions between cumulus convection and other physical processes should provide further guidance in the interpretation of model results.

Sensitivity tests have shown that similar results to the baseline experiment are obtained when different large-scale forcing approaches are used to drive the SCMs. It has also been shown that simulated results can be improved when deficiencies in some aspects of cumulus parametrization are reduced.

REFERENCES

Arakawa, A. and Schubert, W. H.   1974   Interaction of a cumulus cloud ensemble with the large-scale environment. Part I. *J. Atmos. Sci.*, **31,** 674–701

Bechtold, P., Redelsburger, J.-L., Brown, P. R. A., Guichard, F., Hoff, C., Jawasima, M., Lang, S., Montmerle, T., Nakamura, K., Saito, K., Seman, C., Tao, W. K. and Donner, L. J. 2000 A GCSS model intercomparison for a tropical squall line observed during TOGA-COARE. II: Intercomparison of single-column models and a cloud-resolving model. *Q. J. R. Meteorol. Soc.*, **126,** 865–888

Bechtold, P., Bazile, E., Guichard, F., Mascart, P. and Richard, E. 2001 A mass flux convection scheme for region and global models. *Q. J. R. Meteorol. Soc.*, **127,** 869–886

Browning, K. A. 1994 'GEWEX cloud system study (GCSS) science plan'. IGPO Publication Series, No. 11. Available from the International GEWEX Project Office, Reading University, UK

Cederwall, R. T., Krueger, S. K., Xie, S. and Yio, J. 2000 'ARM/GCSS Single Column Model (SCM) Intercomparison, procedures for Case 3: Summer 1997 SCM IOP'. LLNL Report, UCRL-ID-141823. Available from Atmospheric Science division, LLNL, Livermore, California, USA

Cheng, M.-D. and Yanai, M. 1989 Effects of downdrafts and mesoscale convective organization on the heat and moisture budgets of tropical cloud clusters. Part III: Effects of mesoscale convective organization. *J. Atmos. Sci.*, **46,** 1566–1588

Del Genio, A. D. and Yao, M.-S. 1993 Efficient cumulus parameterization for long-term climate studies: The GISS scheme. In *The representation of cumulus convection in numerical models*. Meteorological Monograph 46. Eds. K. Emanuel and D. Raymond. American Meteorological Society Boston, Mass., USA

Del Genio, A. D., Yao, M.-S., Kovari, W. and Lo, K.-W. 1996 A prognostic cloud water parameterization for global climate models. *J. Climate*, **9,** 270–304

Ding, P. and Randall, D. A. 1998 A cumulus parameterization with multiple cloud base levels. *J. Geophys. Res.*, **103,** 11341–11354

Donner, L. J. 1993 A cumulus parameterization including mass fluxes, vertical momentum dynamics, and mesoscale effects. *J. Atmos. Sci.*, **50,** 889–906

Ghan, S. J., Leung, L. R. and Hu, Q. 1997 Application of cloud microphysics to NCAR CCM2. *J. Geophys. Res.*, **102,** 16507–16527

Ghan, S. J., Randall, D. A., Xu, K.-M., Cederwall, R., Cripe, D., Hack, J., Iacobellis, S., Klein, S., Krueger, S. K., Lohmann, U., Pedretti, J., Robock, A., Rotstayn, L., Somerville, R., Stenchikov, G., Sud, Y., Walker, G., Xie, S. C., Yio, J. and Zhang, M.-H. 2000 An intercomparison of single column model simulations of summertime midlatitude continental convection. *J. Geophys. Res.*, **105,** 2091–2124

Gregory, D. 1995 'Convection scheme: Part 1 of UM Documentation'. Paper 27, NWP-Division, Meteorological Office, London Road, Bracknell, Berkshire, UK
                  2001 Estimation of entrainment rate in simple models of convective clouds. *Q. J. R. Meteorol. Soc.*, **127,** 53–72

Gregory, D. and Guichard, F. 2002 Aspects of the parametrization of organized convection: contrasting cloud-resolving model and single-column realizations. *Q. J. R. Meteorol. Soc.*, **128,** 625–646

Gregory, D. and Rowntree, P. R. 1990 A mass flux convection scheme with representation of cloud ensemble characteristics and stability-dependent closure. *Mon. Weather Rev.*, **118,** 1483–1506

Gregory, D., Morcrette, J.-J., Jakob, C., Beljaars, A. M. and Stockdale, T. 2000 Revision of convection, radiation and cloud schemes in the ECMWF Integrated Forecasting System. *Q. J. R. Meteorol. Soc.*, **126,** 1686–1710

Grell, G. A., Kuo, Y.-H., and Pasch, R. 1991 Semiprognostic tests of cumulus parameterization schemes in the middle latitudes. *Mon. Weather Rev.*, **119,** 5–31

Hack, J. J. 1994 Parameterization of moist convection in the National Center for Atmospheric Research Community Climate Model (CCM2). *J. Geophys. Res.*, **99,** 5551–5568

Hack, J. J., Boville, B. A., Briegleb, B. P., Kiehl, J. T., Rasch, P. J. and Williamson, D. L. 1993 'Description of the NCAR Community Climate Model (CCM2)'. NCAR Technical Note, NCAR TN-336-STR. National Center for Atmospheric Research, Boulder, CO, USA

Hack, J. J., Pedretti, J. A. and Petch, J. C. 1998 'SCCM User's Guide'. (http://www.cgd.ucar.edu/cms/sccm/sccm.html) NCAR, Boulder, Colorado, USA

Houze, R. A. and Cheng, C.-P. 1981 Inclusion of mesoscale updrafts and downdrafts in computations of vertical fluxes by ensembles of tropical clouds. *J. Atmos. Sci.*, **38,** 1751–1770

Iacobellis S. F. and Somerville, R. J. C. 2000 Implication of microphysics for cloud–radiation parameterizations: Lessons from TOGA COARE. *J. Atmos. Sci.*, **57,** 161–183

Johnson, R. H. 1980 Diagnosis of convective and mesoscale motions during Phase III of GATE. *J. Atmos. Sci.*, **37,** 733–753

Johnson, R. H. and Hamilton P. J. 1988 The relationship of surface pressure features to the precipitation and airflow structure of an intense midlatitude squall line. *Mon. Weather Rev.*, **116,** 1444–1472

Kiehl, J. T., Boville, B., Briegleb, B., Hack, J., Rasch, P. and Williamson, D. 1996 'Description of the NCAR Community Climate Model (CCM3)'. NCAR Technical Note, NCAR/TN-420+STR. National Center for Atmospheric Research, Boulder, CO, USA

Krueger, S. K. and Lazarus, S. M. 1999 'Intercomparison of multi-day simulations of convection during TOGA COARE with several cloud-resolving and single-column models'. Pp. 643–647 in Preprints to the 23rd conference on hurricanes and tropical meteorology, Dallas, TX. American Meteorological Society, Boston, USA

Lafore, J. P., Stein, J., Asencio, N., Bougeault, P., Ducrocq, V. and Duron, J. 1998 The Meso-NH Atmospheric Simulation System. Part I: Adiabatic formulation and control simulations. *Ann. Geophys.*, **16,** 90–109

Lohmann, U., McFarlane, N., Levkov, L., Abdella, K. and Albers, F. 1999 Comparing different cloud schemes of a single column model by using mesoscale forcing and nudging technique. *J. Climate*, **12,** 438–461

Lord, S. J. and Arakawa, A. 1980 Interaction of a cumulus cloud ensemble with the large-scale environment. Part II. *J. Atmos. Sci.*, **37,** 2677–2692

1982 Interaction of a cumulus cloud ensemble with the large-scale environment. Part III: Semiprognostic test of Arakawa–Schubert cumulus parameterization. *J. Atmos. Sci.*, **39,** 88–103

McFarlane N. A., Boer, G. J., Blanchet, J.-P. and Lazare, M. 1992 The Canadian Climate Center second-generation general circulation model and its equilibrium climate. *J. Climate*, **5,** 1013–1044

Moorthi, S. and Suarez, M. J. 1992 Relaxed Arakawa–Schubert: A parameterization of moist convection for general circulation models. *Mon. Weather Rev.*, **120,** 978–1002

Moran, K. P., Martner, B. E., Post, M. J., Kropfli, R. A., Welsh, D. C. and Widerner, K. B. 1998 An attended cloud-profiling radar for use in climate research. *Bull. Am. Meteorol. Soc.*, **79,** 443–455

Ogura, Y. and Jiang, H.-Y. 1985 A modeling study of heating and drying effects of convective clouds in an extratropical mesoscale convective system. *J. Atmos. Sci.*, **42,** 2478–2492

Pan, D.-M. and Randall, D. A. 1998 A cumulus parametrization with a prognostic closure. *Q. J. R. Meteorol. Soc.*, **124,** 949–982

Pope, V. D., Gallani, M., Rowntree, P. R. and Stratton, R. A. 2000 The impact of new physical parametrizations in the Hadley Centre climate model—HadAM3. *Clim. Dyn.*, **16,** 123–146

Randall, D. A. and Cripe, D. G. 1999 Alternative methods for specification of observed forcing in single-column models and cloud system models. *J. Geophys. Res.*, **104,** 24527–24545

Randall, D. A., Xu, K.-M., Somerville R. J. C. and Iacobellis, S. 1996 Single-column models and cloud ensemble models as links between observations and climate models. *J. Climate*, **9,** 1683–1697

Raymond D. J. 1993 Observational constraints on cumulus parameterization. In *The representation of cumulus convection in numerical models*. Meteorological Monograph 46. Eds. K. Emanuel and D. Raymond. American Meteorological Society, Boston, Mass., USA

Redelsperger, J.-L., Brown, P. R. A., Guichard, F., Hoff, C., Kawasima, M., Lang, S., Montmerle, Th., Nakamura, K., Saito, K., Seman, C., Tao, W. K. and Donner, L. J. 2000 A GCSS model intercomparison for a tropical squall line observed during TOGA-COARE. Part I: CRM results. *Q. J. R. Meteorol. Soc.*, **126,** 823–863

Rotstayn, L. D. 1997 A physically based scheme for the treatment of stratiform clouds and precipitation in large-scale models. I: Description and evaluation of the microphysical processes. *Q. J. R. Meteorol. Soc.*, **123,** 1227–1282

Rotstayn, L. D., Ryan, B. F. and Katzfey, J. J. 2000 A scheme for calculation of the liquid fraction in mixed-phase stratiform clouds in large-scale models. *Mon. Weather Rev.*, **128,** 1070–1088

Stokes, G. M. and Schwartz, S. E. 1994 The Atmospheric Radiation Measurement (ARM) program: Programmatic background and design of the cloud and radiation test bed. *Bull. Am. Meteorol. Soc.*, **75,** 1202–1221

Sud, Y. C. and Walker, G. K. 1993 A rain-evaporation and downdraft parameterization to complement a cumulus updraft scheme and its evaluation using GATE data. *Mon. Weather Rev.*, **121,** 3019–3039

 1999a Microphysics of clouds with the relaxed Arakawa–Schubert scheme (McRAS). Part I: Design and evaluation with GATE phase III data. *J. Atmos. Sci.*, **56,** 3196–3220

 1999b Microphysics of clouds with the relaxed Arakawa–Schubert scheme (McRAS). Part II: Implementation and Performance in GEOS II GCM. *J. Atmos. Sci.*, **56,** 3221–3240

Takacs, L. L., Molod, A. and Weng, T. 1994 'Goddard Earth Observing System (GEOS) general circulation model (GCM) version 1'. NASA Technical Memorandum 104606, Vol. 1. Available from Laboratory for Atmospheres, NASA/Goddard Space Flight Center, Greenbelt, Maryland, USA

Taylor, K. E. 2001 Summarizing multiple aspects of model performance in a single diagram. *J. Geophys. Res.*, **106,** 7183–7192

Thompson, R. M. Jr., Payne, S. W., Recker E. E. and Reed, R. J. 1979 Structure and properties of synoptic-scale wave disturbances in the intertropical convergence zone of the eastern Atlantic. *J. Atmos. Sci.*, **36,** 53–72

Tiedtke, M. 1989 A comprehensive mass flux scheme for cumulus parameterization in large-scale models. *Mon. Weather Rev.*, **117,** 1779–1800

von Salzen, K. and McFarlane, N. A. 2002 Parameterization of the effects of lateral and cloud-top entrainment in transient shallow cumulus clouds. *J. Atmos. Sci.*, **59,** 1405–1430

Webster, P. J. and Lukas, R. 1992 TOGA COARE: The coupled ocean–atmosphere response experiment. *Bull. Am. Meteorol. Soc.*, **73,** 1377–1417

Wu, X. 1993 Effects of cumulus ensembles and mesoscale stratiform clouds in midlatitude convective systems. *J. Atmos. Sci.*, **50,** 2496–2518

Xie, S. C. and Zhang, M. H. 2000 Impact of the convective triggering function on single-column model simulations. *J. Geophys. Res.*, **105,** 14983–14996

Xu, K.-M. 1995 Partitioning mass, heat and moisture budgets of explicitly simulated cumulus ensembles into convective and stratiform components. *J. Atmos. Sci.*, **52,** 551–573

Xu, K.-M. and Arakawa, A. 1992 Semi-prognostic tests of the Arakawa–Schubert cumulus parameterization using simulated data. *J. Atmos. Sci.*, **49,** 2421–2436

Xu, K.-M. and Randall, D. A. 2000 Explicit simulation of midlatitude cumulus ensembles: comparison with ARM data. *J. Atmos. Sci.*, **57,** 2839–2858

Xu, K.-M., Cederwall, R. T., Donner, L. J., Grabowski, W. W., Guichard, F., Johnson, D. E., Khairoutdinov, M., Krueger, S. K., Petch, J. C., Randall, D. A., Seman, C. J., Tao, W.-K., Wang, D., Xie, S. C., Yio, J. and Zhang, M.-H. 2002 An intercomparison of cloud-resolving models with the Atmospheric Radiation Measurement summer 1997 Intensive Observation Period data. *Q. J. R. Meteorol. Soc.*, **128,** 593–624

Yanai, M., Esbensen, S. and Chu, J. 1973 Determination of bulk properties of tropical cloud clusters from large-scale heat and moisture budgets. *J. Atmos. Sci.*, **30,** 611–627

Yanai, M., Chu, J., Stark, T. E. and Nitta, T. 1976 Response of deep and shallow tropical maritime cumuli to large-scale processes. *J. Atmos. Sci.*, **33,** 976–991

Zhang, G. J. 2002 Convective quasi-equilibrium in midlatitude continental environment and its effect on convection parameterization. *J. Geophys. Res.*, in press

Zhang, G. J. and McFarlane, N. A. 1995 Sensitivity of climate simulations to the parameterization of cumulus convection in the Canadian Climate Center general circulation model. *Atmos.–Ocean*, **33,** 407–446

Zhang, M. H. and Lin, J. L. 1997 Constrained variational analysis of sounding data bases on column-integrated budgets of mass, heat, moisture, and momentum: Approach and application to ARM measurements. *J. Atmos. Sci.*, **54,** 1503–1524

Zhang, M. H., Lin, J. L., Cederwall, R. T., Yio, J. J. and Xie, S. C. 2001 Objective analysis of ARM IOP data: Method and sensitivity. *Mon. Weather Rev.*, **129,** 295–311